

The Spectrum of Fault Slip in Elastoplastic Fault Zones

Md Shumon Mia^{1,2}, Mohamed Abdelmeguid^{2,3}, Ahmed E. Elbanna^{2,4}

¹Department of Mechanical Science and Engineering, University of Illinois at Urbana-Champaign, Urbana, IL, USA.

²Department of Civil and Environmental Engineering, University of Illinois at Urbana-Champaign, Urbana, IL, USA.

³Graduate Aerospace Laboratories, California Institute of Technology, Pasadena, CA, USA.

⁴Beckman Institute of Advanced Science and Technology, University of Illinois at Urbana-Champaign, Urbana, IL, USA.

Corresponding author: Md Shumon Mia (mmia2@illinois.edu)

This is a preprint submitted to Earth and Planetary Science Letters.

Highlights:

- Numerical models for inelastic fault zones showing the spectrum of fault slip.
- New stability transition boundary depending on yield strength.
- Transition from fast to slow slip with increased bulk inelastic dissipation.
- Complete locking of seismogenic patch with lower yield strength.

16 **Abstract**

17 Natural faults are typically surrounded by damage zones that exhibit inelastic material response.
18 This study investigates the role of fault zone strength in modulating the spectrum of fault slip
19 across different spatio-temporal scales. We carry out long-term simulations of seismic and
20 aseismic slip for an elastoplastic spring slider model with rate-and-state friction as well as a
21 continuum model of a 2D anti-plane rate-and-state fault embedded in an elastoplastic bulk. Results
22 of the elastoplastic spring slider model show the emergence of a new stability boundary, depending
23 on the bulk yield strength relative to fault frictional strength, that limits the rupture size regardless
24 of the fault length. Continuum simulations generate a spectrum of slip analogous to the spring
25 slider model including localized or migrating events of slow and fast slip. A fault may remain
26 locked for yield strength sufficiently low and close to fault reference strength even if it is
27 intrinsically rate weakening and larger than the nucleation length scale predicted by the elastic
28 analysis. These findings shed new light on the nature of fault frictional stability and suggest the
29 critical role of the fault zone rheological properties in modulating the spectrum of fault slip.

30 **1. Introduction**

31 Unstable sliding of geologic faults manifests itself as earthquakes—one of the deadliest and most
32 prevalent yet unpredictable natural hazards. Apart from large earthquakes, faults are also found to
33 host small earthquakes and slow slip events (Beroza & Ide, 2011; Ito et al., 2013; Burgmann 2018).
34 Usually, earthquakes are associated with frictional sliding on fault surfaces encompassing long-
35 term slow aseismic slip and rapid seismic ruptures (Avouac 2015). However, fault zone
36 complexities, including geometric and material non-linearity (Ben-Zion & Sammis, 2003; Mitchell
37 & Faulkner, 2009; Lewis & Ben-Zion, 2010), influence the fault slip behavior leading to complex
38 patterns of seismicity in space and time (Chen et al., 2020; Ross et al., 2020). Physics-based

39 simulations for sequences of earthquakes and aseismic slip (Ben-Zion & Rice, 1993; Lapusta et
40 al., 2000; Chen & Lapusta 2009; Kaneko et al., 2010; Barbot et al., 2012; Allison & Dunham,
41 2021; Erickson et al., 2022; Jiang et al., 2022; Abdelmeguid & Elbanna, 2022a, 2022b) are
42 emerging as promising tools for understanding the complex processes associated with different
43 forms of frictional instabilities and resulting slip pattern, as well as in developing seismic hazard
44 models.

45 Stable and unstable frictional sliding is largely attributed to the frictional properties of the fault
46 whether the steady-state frictional strength increases with slip rate (velocity strengthening) or
47 decreases with slip rate (velocity weakening). A velocity-strengthening patch is generally
48 associated with stable aseismic sliding and may become unstable through enhanced coseismic
49 weakening associated with flash heating or a rapid increase in pore fluid pressure due to shear
50 heating (Noda & Lapusta, 2013). While a fault with velocity-weakening friction is locked during
51 the interseismic period, it is potentially unstable and generates different patterns of slip. The style
52 of slip in terms of peak slip rate, spatial extent, and temporal periodicity, depends on the size of
53 the velocity weakening patch relative to the critical length scale associated with nucleation as well
54 as the relative magnitude of frictional parameters associated with static and dynamic stress drop
55 (Barbot 2019; Cattania 2019). Generation of slow slip sequence accompanied by slow earthquakes
56 are shown in Barbot (2019) to depend on the relative magnitude of the frictional parameters and
57 the relative fault size. Specifically, slow slip is found in these studies when the length of the
58 velocity weakening patch is close to the nucleation length.

59 Experimental studies (Leeman et al., 2016; Scuderi et al., 2016) show emergence of spectrum of
60 slip controlled by the ratio between the elastic stiffness (k) of the loading medium and the critical
61 stiffness (k_c) governed by frictional rheology. Stable sliding corresponds to $\frac{k}{k_c} > 1$ and fast stick-

62 slip instability occurs with $\frac{k}{k_c} \ll 1$. Slow slip is observed near the transition between stable and
63 unstable sliding with $\frac{k}{k_c} \sim 1$. These results conform with the stability analysis of spring slider model
64 with rate-and-state friction (Ranjith & Rice, 1999) and provide a possible explanation for the
65 spectrum of fault slip considering the off-fault bulk as elastic.

66 Geologic heterogeneities observed along natural faults (Fagereng & Sibson, 2010; Collettini et al.,
67 2019) can play a role in generating different styles of slip including slow slip and fast rupture.
68 Skarbek et al. (2012) shows that geologic heterogeneity in terms of the different proportions of
69 velocity strengthening and velocity weakening patches may give rise to slow slip. Small scale
70 heterogeneity in fault gauge inferred from laboratory friction experiment (Bedford et al., 2022) is
71 shown to influence frictional stability through reduction in fault strength with increased
72 heterogeneity. Also, the rate-dependent evolution (Kaproth & Marone, 2013) of frictional
73 parameters is a possible mechanism for slow slip generation. Velocity-weakening friction
74 generating stick-slip instabilities may generate slow slip when rate-and-state friction parameters
75 evolve with slip rate and take transition from velocity weakening to velocity strengthening.
76 Numerical simulations using a spring-slider model by Im et al. (2020) show that velocity
77 dependent frictional parameters enable generating slow slip events having similar characteristics
78 to those observed in nature (Dragert et al., 2001; Heki & Kataoka, 2008; Radiguet et al., 2012).
79 However, it is not clear what physical mechanism may lead to this rate dependence of the frictional
80 parameters.

81 Pore pressure also plays an important role in controlling spectrum of slip. Fluid pressure reduces
82 effective normal stress and increases the nucleation length scale. Accordingly, the size of the
83 seismogenic velocity-weakening patch decreases relative to the size of the nucleation patch. This

84 results in slow slip transients (Liu & Rice, 2007). Dilatant strengthening (Segall et al., 2010),
85 resulting in reduced pore pressure, also explains the generation of slow slip events in a seismogenic
86 velocity-weakening region. Slow and fast slip may arise through the relative contribution of
87 dilatancy-induced strengthening and enhanced coseismic weakening due to thermal pressurization
88 of pore fluid. Dilatant hardening itself may be a manifestation of inelastic processes associated
89 with propagating crack tip (French & Zhu, 2017).

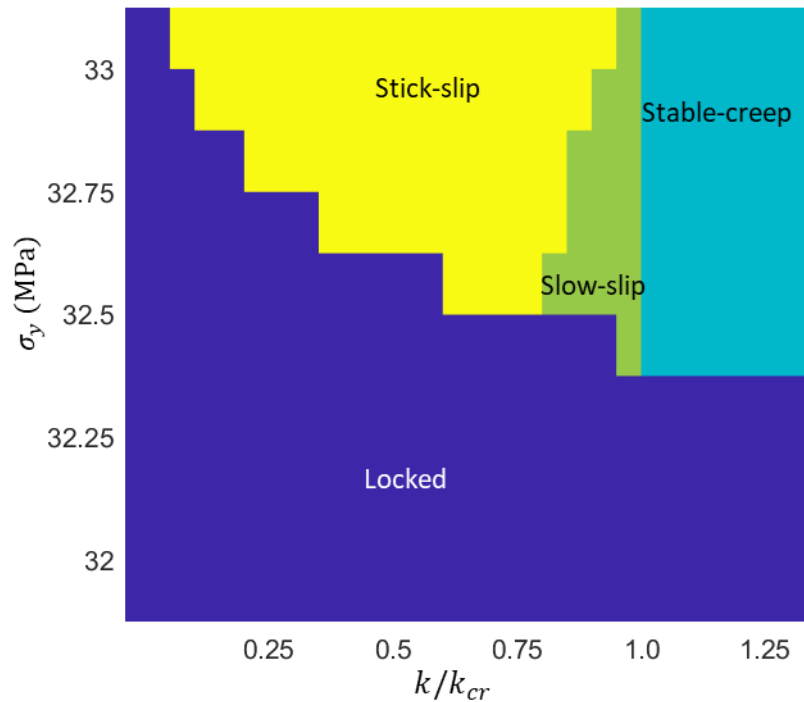
90 These on-fault characteristics controlling the spectrum of slip are investigated mostly with
91 homogeneous elastic bulk. Heterogenous bulk with a low velocity zone near the fault may generate
92 slip complexity (Abdelmeguid 2019; Thakur et al. 2020; Nie & Barbot 2022). Also, a recent study
93 by Collettini et al. (2022) explains the observation of distributed microseismicity through a
94 conceptual model of distributed ductile deformation in the bulk. Incorporation of viscoelastic fault
95 zones (Miyake & Noda, 2019; Goswami & Barbot, 2018) and viscous damping in fault strength
96 (Wu 2021; Nakata et al., 2011) are shown to generate slow slip events. Erickson et al. (2017)
97 models earthquake cycle in rate-and-state fault with off-fault plasticity. They show partitioning of
98 deformation and resulting slip deficit with off-fault plasticity accumulation near the free surface
99 of a vertical fault. However, the resulting pattern of seismicity with off-fault plasticity is similar,
100 in their study, to the homogeneous elastic case having periodic seismic events. Using numerical
101 simulation with elastoplastic shear zone, Tong & Lavier (2018) shows generation of slow and fast
102 slip events by varying the rate-and-state friction parameters. By reducing the difference between
103 the direct effect parameter and state evolution parameter, they found slip pattern to change from
104 fast slip events to slow slip. In the limit of vanishing difference between the friction parameters,
105 corresponding to the limit of velocity neutral, creeping events are found.

106 In our previous work on seismic cycle simulations with off-fault plasticity (Mia et al., 2022), we
107 showed that bulk yield strength and post-yield viscous relaxation contribute to the emergence of
108 spatio-temporal clustering of seismicity. Here, we investigate the effect of off-fault bulk strength
109 on fault slip expanding the parameter space for yield strength to also consider values close to the
110 reference frictional strength. This is a critical parameter regime that have not been investigated
111 before and may qualitatively alter the partitioning of slip and energy dissipation between on-fault
112 and off-fault processes. To that end, we first simulate the long-term frictional sliding of an
113 elastoplastic spring slider model with rate-and-state friction. Then, to further corroborate our
114 findings, we investigate sequences of seismic and aseismic slip on a 2D anti-plane rate and state
115 model embedded in a fully continuum elastoplastic model. We evaluate the resulting slip patterns
116 with a special focus on slow slip.

117 **2. Elastoplastic spring slider**

118 We simulate the long-term sliding of a spring-block system under constant load-point velocity
119 applied at the end of the spring. The details of the spring slider model are outlined in the
120 Supplementary Information (Figure-S1, Text-S2). The spring with stiffness (k) and yield strength
121 (σ_y) idealize the bulk material with elastoplastic response. The frictional interface represents a
122 fault surface with uniform friction. The friction here is velocity weakening governed by rate-and-
123 state friction law (Dieterich, 1979; Ruina, 1983) and the state evolution follows the aging law
124 (Dieterich, 1978; Ruina, 1983; Ben-Zion & Rice, 1997; Ampuero & Rubin, 2008). The friction
125 law is outlined in the Supplementary Information (Text-S1). To investigate the effect of bulk
126 strength on frictional sliding, we vary the yield strength (σ_y) and the stiffness (k) of the spring.
127 Critical stiffness (Rice & Ruina, 1983; Ranjith & Rice, 1999) is related to the frictional properties
128 and normal stress (σ_n), and is defined by, $k_{cr} = \sigma_n(b - a)/L$. Where, a , and b are non-negative

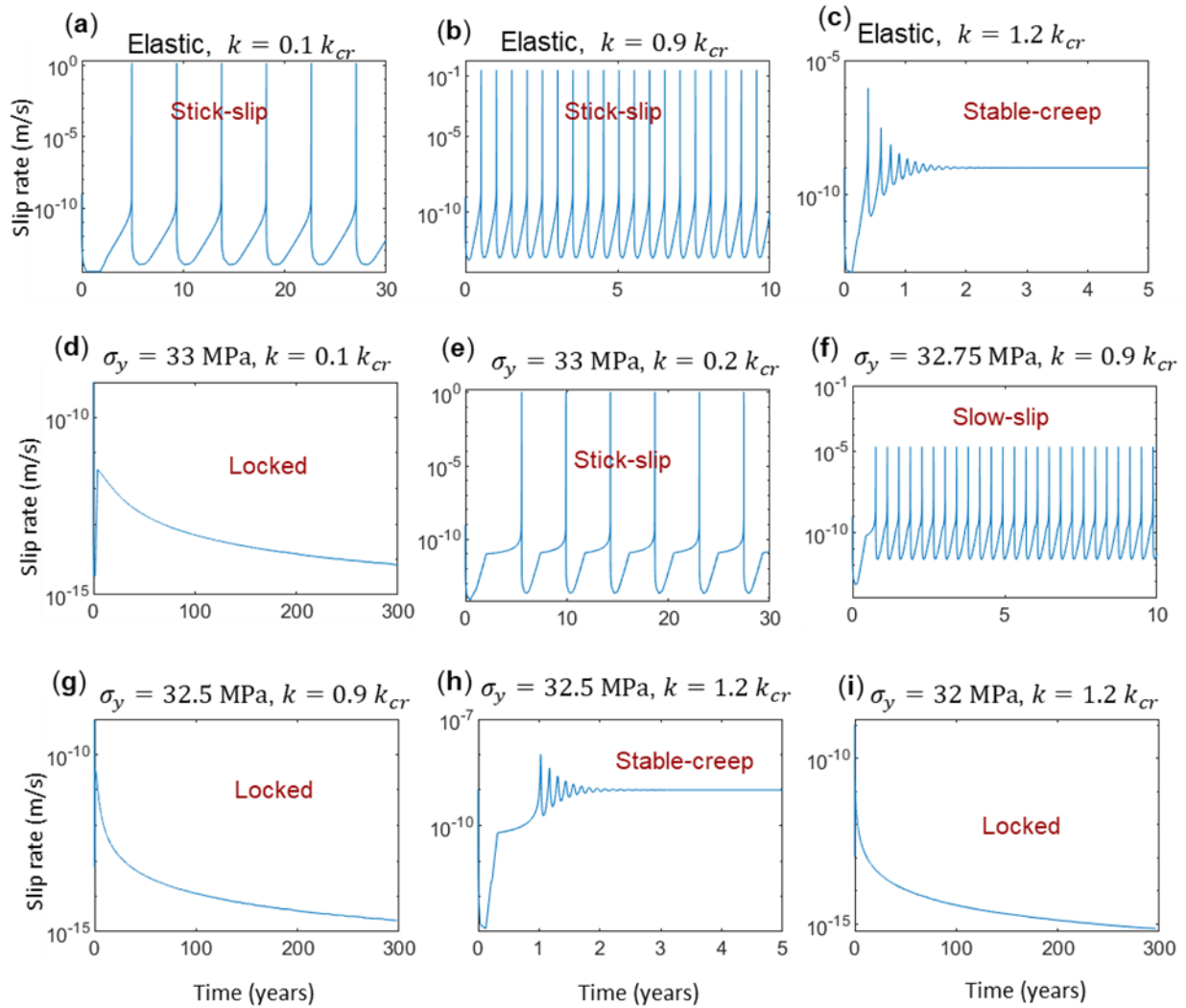
129 dimensionless parameters associated with rate-and-state friction law. At steady state, $(b - a)$
 130 defines the velocity dependence of friction coefficient with $(b - a) > 0$ indicates that steady-state
 131 friction decreases with the increase in the sliding velocity, i.e., velocity-weakening response. L is
 132 the characteristic slip distance. Critical stiffness marks the transition between stable and unstable
 133 frictional sliding in a purely elastic setting.



134
 135
 136 **Figure 1.** Sliding patterns for an elastoplastic spring block system depending on yield strength (σ_y) and stiffness (k)
 137 of the spring. Reference strength of the frictional interface is $\sigma_n f_o = 30 \text{ MPa}$. Sliding patterns change from stick-slip
 138 to slow-slip as spring stiffness becomes close to a critical stiffness defined for the elastic system from the frictional
 139 parameters as $k_{cr} = \sigma_n (b - a) / L$. For stiffness higher than critical value, the sliding is stable. A region of slow-slip
 140 exists between stick-slip and stable-creep for a narrow range of stiffness and yield strength values. There is another
 141 transition towards lower stiffness, which depends on the magnitude of the yield strength, where the slider remains
 142 locked. This new stability boundary does not exist for purely elastic spring block systems.

143 From stability analysis (Ranjith & Rice, 1999; Rice et al., 2001), it is known that stiffness greater
 144 than the critical value corresponds to stable sliding which tends to attain steady state in sync with
 145 the imposed load point velocity. For elastic spring, stiffness lower than the critical value generate
 146 unstable sliding. The elastoplastic spring block slider shows different sliding patterns ranging from

147 stick-slip to complete locking depending on the yield strength and the elastic stiffness of the spring
148 (Figure-1). The slip rate vs. time plots for selected values of yield strength and spring stiffness are
149 presented in Figure-2. We classify the slip patterns based on the amplitude of the block's peak slip
150 rate (Goswami & Barbot, 2018; Tong & Lavier, 2018; Miyake & Noda, 2019). Slow slip is
151 identified with slip rate lower than a seismic threshold (taken here to be 0.01 m/s) but higher than
152 the background plate rate (10^{-9} m/s). Stick slip corresponds to slip rate exceeding the seismic
153 threshold. We observe that slow slip emerges for a narrow range of yield strength and stiffness
154 values (Figure-1). The block also creeps stably at the imposed loading rate for stiffness values
155 larger than the critical value predicted by the elastic analysis. However, as shown in Figure-1,
156 another new transition boundary emerges with plasticity, in the limit of lower stiffness, that is not
157 observed in purely elastic analysis. This transition from stick-slip to locking (i.e., sliding with slip
158 rates that are orders of magnitudes slower than the imposed plate loading rate) depends on the
159 yield strength. As yield strength decreases, this transition stiffness increases. For sufficiently low
160 yield strength, as it becomes close to the reference frictional strength ($\sigma_n f_o$), the slip rate
161 asymptotically decreases to $\sim 10^{-15}$ m/s, orders of magnitude lower than the imposed plate rate.
162 We refer to the sliding with this negligible slip rate as locked.



164

165

166 **Figure 2.** History of slip rate demonstrating various sliding pattern for the spring slider model with different values
 167 of yield strength (σ_y) and elastic stiffness (k). The elastic case (shown in **a-c.**) corresponds to stability transition from
 168 stick-slip to stable-creep when stiffness exceeds a critical value ($k > k_{cr}$). For stick-slip instability, slip rate exceeds
 169 a seismic threshold (taken 0.01m/s here), and for stable-creep, slip rate decays to applied plate rate (10^{-9} m/s). For
 170 the elastoplastic spring (shown in **d-i**), another stability transition appears depending on the magnitude of yield
 171 strength where the slider remains locked (shown in **d, g, i**) as the slip rate is several orders of magnitude lower than
 172 the plate rate. Slip rate lower than the seismic threshold but greater than plate rate corresponds to slow slip as shown
 173 in **f**.

174 3. Continuum simulation of a 2D anti-plane rate-and-state fault

175 We model a 2D anti-plane rate-and-state fault embedded in a full-space elastoplastic medium
 176 subjected to slow tectonic plate rate. The fault has a central velocity-weakening (VW) region
 177 surrounded by velocity-strengthening (VS) patches from both sides (Supplementary Figure-S2).

178 The length of the VW patch is around 5 times the nucleation length. We model off-fault material
179 response with J2 plasticity which coincides with Drucker-Prager plasticity for the anti-plane
180 setting with no variations in normal stress. We further assume no plastic hardening. In this study,
181 we consider the elastoplastic response as a proxy for isotropic microscale damage. While damage
182 processes may also produce time-dependent changes in the elastic moduli through degradation and
183 healing, as well as anisotropic material response, we ignore these changes in this study. We
184 elaborate on this approximation in the discussion section. A hybrid scheme combining finite
185 element and spectral boundary integral is employed for spatial discretization (Abdelmeguid et al.,
186 2019; Mia et al., 2022; Abdelmeguid & Elbanna 2022b). We use an adaptive time-stepping
187 algorithm (Lapusta et al. 2000) to efficiently resolve slow and fast slip. The model geometry with
188 the hybrid scheme setup as well as the input parameters for the simulations are outlined in the
189 Supplementary Information (Text-S3, Table-S1, Figure-S2).

190 We simulate sequences of earthquakes and aseismic slip (SEAS) with different values of yield
191 strength to investigate the effect of bulk strength on long-term fast and slow slip. Resulting
192 patterns, given as space-time contours of the fault slip rate, with different values of yield strength
193 are shown in Figure-3. The temporal evolution of the peak slip rate in different cases is shown in
194 Figure-4. The simulations show sliding patterns analogous to the elastoplastic spring slider model.
195 For lower yield strength the fault remains locked without generating any seismic event. When the
196 yield strength is increased, the fault generates unstable frictional sliding including slow slip,
197 spatially localized seismic events, and partial ruptures distributed over the fault length intermixed
198 with transient episodes of slow slip. For higher values of yield strength, or in the limit of purely
199 elastic bulk, the fault fails in predominantly large, fault-spanning, fast earthquakes. Below we
200 briefly describe these different slip regimes.

201 **Locked fault:** When the yield strength (31 MPa) is close to the fault reference frictional strength
202 ($\sigma_n f_o = 30$ MPa), the slip rate of the central VW patch decreases to $\sim 10^{-15}$ m/s (Figure-3a).

203 The instantaneous and steady-state frictional strength for such low slip rate is higher than the
204 reference frictional strength. Relative to the plate loading rate, this slip rate is orders of magnitude
205 smaller which indicates that the seismogenic zone (VW patch) of the fault remains effectively
206 locked or stuck. The VS patch of the fault creeps following the plate loading. Aseismic creep from
207 the VS patch penetrates slightly into the VW patch but the peak slip rate remains close to the
208 imposed plate rate (10^{-9} m/s) in a very limited region adjacent to the VS patch as shown in
209 Figure-3a and Figure-4a.

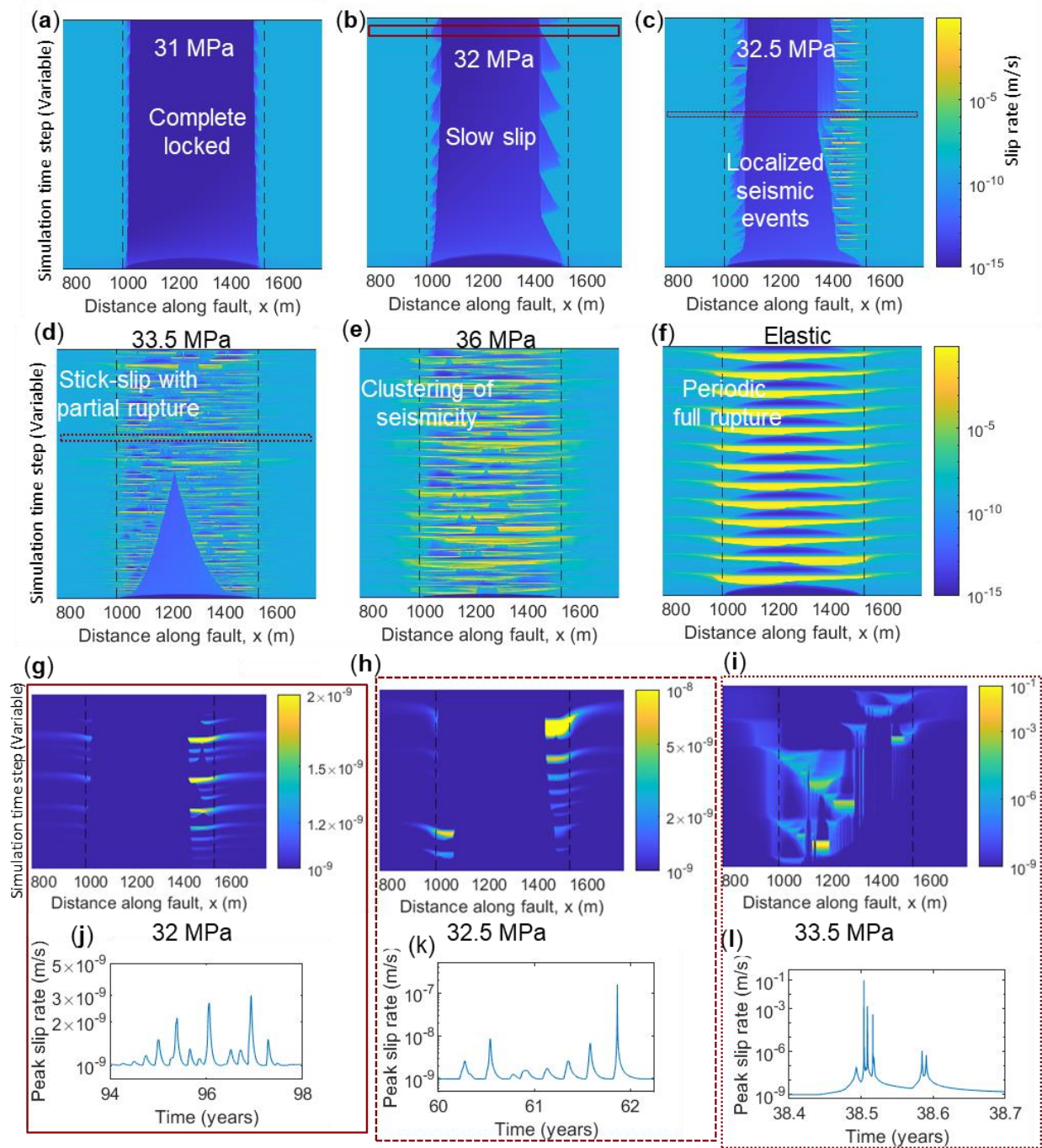
210 **Slow slip:** When the yield strength is increased to 32 MPa, slow slip emerges (Figure-3b, 3g, 3j).
211 Signature of creep penetration exists near the transition between the VS and VW patches. The
212 duration of the slow slip events for yield strength 32 MPa is in the scale of weeks to month.
213 Spatially, these events are localized near the transition region from VS to VW. Similar spatially
214 localized slow slip events are also observed in between localized partial ruptures for yield strength
215 32.5 MPa (Figure-3c, 3h, 3k). However, the peak slip rate associated with some of these aseismic
216 transients reaches orders of magnitude higher than the background plate rate. The irregular pattern
217 with yield strength 33.5 MPa also includes slow slip events (Figure-3d, 3i, 3l). The peak slip rates
218 associated with these slow slip events are even higher, but they are still below the seismic
219 threshold. These slow slip events, observed with yield strength 33.5 MPa, are no longer localized
220 in the transition region. Rather they show spatial migration over the full length of the seismogenic
221 (Velocity-Weakening) patch of the fault.

222 **Localized seismic events:** A repeating pattern of localized seismic events is observed for yield
223 strength 32.5 MPa as shown in Figure-3c. These seismic events are inter-mixed with slow slip
224 episodes as described above. The seismic events are spatially localized near the boundary between
225 VS and VW. They rupture approximately the same area, but they do not repeat with the exact
226 return period (Figure-4c). Their average stress drop is around 2.3 MPa with standard deviation of
227 0.5 MPa approximately which is consistent with stress drop measured for earthquake repeaters

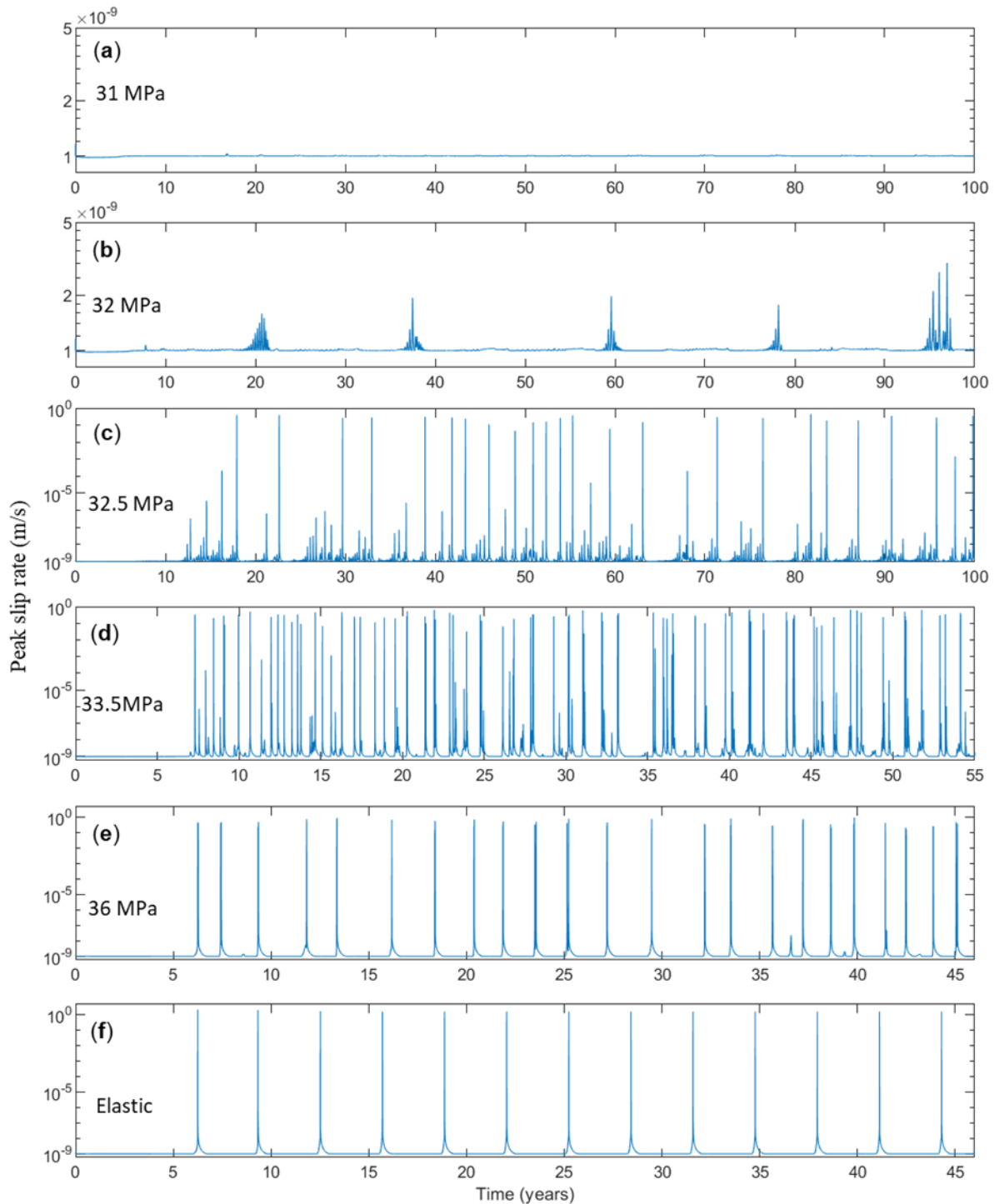
228 (Chen & Lapusta, 2009). The slow slip events observed in this case occur mostly before the seismic
229 events.

230 **Stick-slip with partial ruptures:** When yield strength is increased to 33.5 MPa, fault sliding
231 includes slow slip and partial seismic ruptures (Figure-3d). In the early stages of the sequence,
232 partial ruptures extend on both sides of fault, but a locked patch remains in the center that gets
233 progressively narrower with time. Later in the cycle, the whole VW region is ruptured by
234 subsequent partial events. Here the partial ruptures are prevalent throughout the VW patch unlike
235 the localized repeating events shown in Figure-3b. Also, the clustering of events observed with
236 relatively higher yield strength e.g., 36 MPa (Figure-3e) is not found for the case with yield
237 strength 33.5 MPa.

238 **Stick-slip with fault-spanning ruptures:** For relatively higher yield strength (e.g., 36 MPa
239 shown in Figure-3e), seismic events, including partial ruptures as well as ruptures spanning the
240 full VW patch, dominate the slip pattern. Evolution of the spatial extent of rupture, discussed above
241 for lower yield strength, showing central locked patches progressively unclamped with time does
242 not exist with relatively higher yield strength. The resulting sequence, including partial and fault-
243 spanning rupture, is aperiodic with clustering of seismic events in space and time. Simulation with
244 elastic bulk (Figure-3f) results in simple periodic cycle with fault-spanning ruptures only. Cycle
245 simulations for a range of high values of yield strength and post-yield viscosity are discussed in
246 our previous study (Mia et al., 2022) where seismicity pattern changes from complex spatio-
247 temporal clustering to simple periodic pattern with increasing yield strength and post-yield
248 viscosity. While here we adopted a quasi-dynamic approximation of inertia effect through a
249 radiation damping term, the results are qualitatively similar even if we consider full inertia effects
250 (Supplementary Information, Figure-S3).



251
 252 **Figure 3.** Spectrum of slip for a rate-and-state fault. Spatio-temporal evolution of slip rate illustrating different slip
 253 pattern for different yield strength (a-e). Elastic case results in periodic seismic cycle as shown in f. Region between
 254 two vertical dashed lines correspond to velocity weakening friction. Fault reference strength is $\sigma_n f_o = 30$ MPa. Fault
 255 remains locked for yield strength, $\sigma_y = 31$ MPa. Locked fault with occasional slow slip is found for $\sigma_y = 32$ MPa .
 256 Localized earthquakes near the transition between VS and VW are shown in c. Complex pattern including slow slip
 257 and seismic events with partial rupture is shown in d. Clustering of seismicity is found when yield strength is increased
 258 (e). Closer examination of example of slow slip events that exist with $\sigma_y = 32, 32.5$ and 33.5 MPa are shown in g-l.



260

261

262 **Figure 4.** History of peak slip rate for 2D continuum simulations with different yield strengths (a-e). The elastic
 263 reference case is generating periodic pattern is shown in f. Peak slip rate remains close to the plate rate for locked fault
 264 with yield strength 31 MPa as shown in a. However, this peak slip rate is limited to the VS region. The slip rate in the
 265 VW region drops to 10^{-15} m/s. (b) Slow slip events with 32 MPa. (c) Localized seismic events and preceding slow
 266 slip events with 32.5 MPa. (d) Irregular pattern including slow slip and partial rupture with 33.5 MPa. (e) Aperiodic
 267 sequence with clustering of seismicity for higher yield strength.

268 **Partitioning of deformation**

269 Plasticity results in a slip deficit on the fault surface through partitioning of total deformation into
270 on-fault slip and off-fault plastic deformation. In Figure-5, the spatial distribution of the
271 cumulative slip and off-fault plastic deformation is shown for yield strength 33.5 MPa. Here we
272 calculate an effective measure for the variation of the plastic deformation in the fault zone along
273 the fault length by integrating the equivalent plastic strain, γ , as $u_p(x, t) = 2 \int_0^{L_y} \gamma(x, y, t) dy$,
274 where, L_y is the half width of the computational strip modeled using FEM, and y represents the
275 spatial direction normal to the fault plane. The factor of 2 accounts for the symmetry of the plastic
276 strain distribution about the fault surface. This is characteristics of anti-plane plasticity in
277 homogeneous media where the normal stress does not change with deformation. For the current
278 model geometry, $L_y = 30$ m which is around 1.5 times the process zone size. This width is found
279 sufficient to contain the spatial extent of plasticity in the fault normal direction. Outside this
280 computational strip, the exterior half-spaces are elastic and are modeled using the spectral
281 boundary integral approach. Therefore, they do not experience plastic deformation. Total plastic
282 deformation along the fault, $u_p(x, t)$ is shown in Figure-5b. Cumulative slip is plotted in Figure-
283 5a. The contour lines for both quantities are plotted every 10 years up to 50 years.

284 As shown in Figure-5a, cumulative slip in the VS patch is around 1.5 m in 50 years. Slip
285 accumulation is reduced near the transition from VS to VW and is further reduced in the interior
286 of the locked VW region. The central region of the VW patch is locked in early stages. As time
287 passes, seismic events progressively unlock the VW fault through a sequence of partial ruptures
288 as shown in Figure-3d. The non-smooth shape of the cumulative slip lines corresponds to the
289 irregular pattern of slow slip and partial ruptures spreading over the whole VW region. From the

290 plastic deformation plot (Figure-5b), it is evident that plastic deformation in the bulk compensates
291 for the slip deficit in the VW patch. Plastic deformation is maximum in the central part of the VW
292 patch where the fault slip is minimum and gradually vanishes towards the VS region.

293 Off-fault plastic deformation gets an increasing share of the total deformation budget when the
294 bulk yield strength is lower. To evaluate the partitioning of deformation and associated slip pattern
295 for different values of yield strength, we compute the on-fault deformation by integrating fault slip
296 termed as Potency (t) = $\int_0^{L_f} d(x, t)dx$, and off-fault plastic deformation by integrating the
297 equivalent plastic strain over the domain as $PD(t) = \int_S \gamma(x, y, t)dS$. Where d is the slip, L_f is
298 the seismogenic region of the fault including VW patch and the transition region between VW and
299 VS, and S is the area of the 2D elastoplastic fault zone. For all the cases shown in Figure-5c, there
300 is an initial increase of plastic deformation while the potency is small. This indicates plasticity
301 accumulation when the fault is locked prior to any seismic events. When fault slip occurs, both
302 potency and plastic deformation increases but the increment of plastic deformation is relatively
303 lower. For the cases shown in Figure-5c, the ratio between plastic deformation and potency varies
304 over an order of magnitude ranging from ~ 0.1 for $\sigma_y = 36$ MPa to ~ 3.5 for $\sigma_y = 32$ MPa.

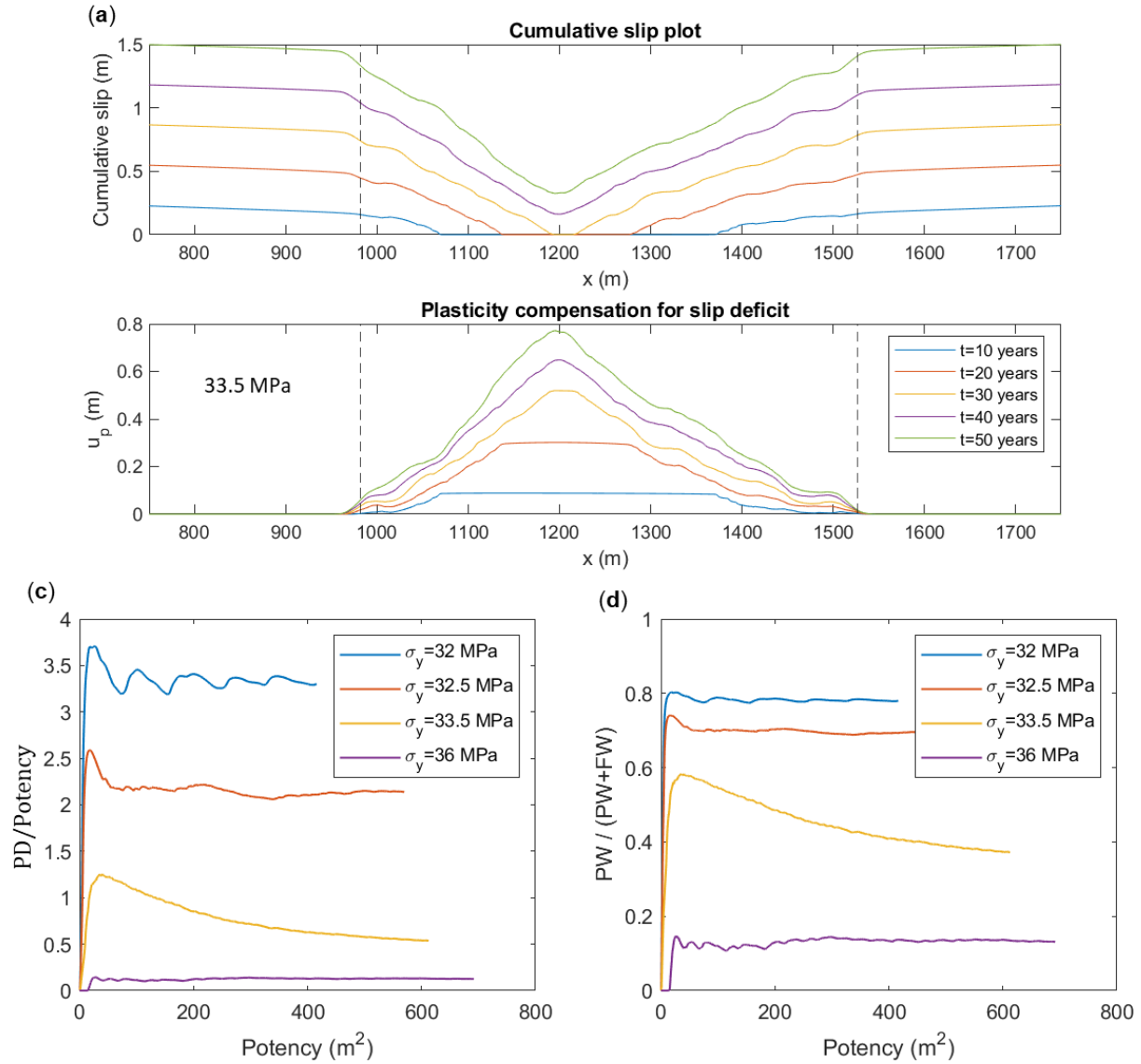
305 For the same amount of potency, plastic deformation is higher with lower yield strength. The
306 pattern of slip with clustered seismic events ($\sigma_y = 36$ MPa , shown in Figures-3,5) is associated
307 with relatively lower plastic deformation to potency ratio (~ 0.1). However, fault slip involving
308 slow slip and partial ruptures spreading over the fault ($\sigma_y = 33.5$ MPa , shown in Figures-3,5)
309 correspond to higher ratios of plastic deformation to potency (~ 0.5). Localized seismic event and
310 slow slip in otherwise locked fault ($\sigma_y = 32.5$ MPa, $\sigma_y = 32$ MPa shown in Figures-3,5)

311 corresponds to relatively higher plastic deformation to potency ratio (> 1). In these limits of low
312 yield strength, more deformation is distributed in the bulk than localized as slip on the fault surface.

313 Figure-5d shows the ratio of plastic dissipation relative to total dissipation. Total dissipation is the
314 sum of plastic dissipation (PW) and frictional dissipation (FW). Here, frictional dissipation is
315 computed over the region of the fault used to compute the potency. This region includes the VW
316 patch as well as the transition regions between the VW and VS patches. That is, we do not account
317 for frictional dissipation due to slip in the VS region which conforms to the plate loading.

318 Contribution of plastic dissipation is higher with lower yield strength. On one hand, for the case
319 of $\sigma_y = 32$ MPa , generating slow slip events, plastic dissipation is around 80% of the total
320 dissipation. On the other hand, clustered seismic events with $\sigma_y = 36$ MPa is associated with much
321 lower plastic dissipation ($\sim 10\%$ of total dissipation). The decrease in the ratio of plastic to total
322 dissipation is a result of less off-fault plastic deformation and corresponds to higher frictional
323 dissipation through fault slip in large and fast seismic events. Higher off-fault deformation and
324 smaller on-fault slip leads to increased off-fault dissipation. Mia et al., 2022, showed that even if
325 the contribution of plasticity to the energy budget is small, it may still play a significant role in
326 regulating the spatio-temporal clustering of seismic events through limiting the stress
327 concentration ahead of the rupture tip and facilitating rupture arrest. Here, we additionally show
328 that if the energy dissipation is dominated by off-fault plastic dissipation, which happens for lower
329 yield strength, fault-spanning events cannot occur, and slip becomes progressively slower.

330 Specifically, we observe that irregular partial ruptures, slow slip, repeaters, and even complete
331 locking of the VW patch emerge in the limit of low yield strength and increased off-fault plastic
332 dissipation irrespective of fault length. This further suggests that plastic dissipation should be low
333 (less than 10%) compared to total dissipation, for large fault spanning events to occur.



334
 335 **Figure 5.** Plasticity compensation for slip deficit and partitioning of deformation as well as energy dissipation between
 336 the bulk and the fault. (a) Cumulative slip is plotted at an interval of 10 years (for $\sigma_y = 33.5$ MPa). (b) Off-fault
 337 plastic deformation obtained from integrating the plastic strain in lateral direction is plotted along the fault in the same
 338 interval of cumulative slip plot (for $\sigma_y = 33.5$ MPa). The region within the two vertical dashed lines corresponds to
 339 the fault section with velocity weakening friction. The extent of locked region subsequently shrinks with increased
 340 slip. Plasticity compensation is higher in the region where slip accumulation is lower. (c) Relative contribution of on-
 341 fault slip and off-fault plastic deformation. Potency is computed by integrating slip, $Potency(t) = \int_0^{L_f} d(x, t) dx$ and
 342 plastic deformation is computed from integrating the plastic strain over the domain, $PD(t) = \int_S \gamma(x, y, t) dS$. Lower
 343 yield strength corresponds to higher amount of plastic deformation. (d) Plot of plastic energy dissipation (PW)
 344 relative to total dissipation. FW is the frictional dissipation computed over the velocity weakening patch and the transition
 345 region. Higher percentage of plastic dissipation is associated with lower yield strength generating slow slip.

346 **4. Discussion**

347 In this work, we showed, using a simple elastoplastic spring block model, that spring stiffness,
348 even when lower than the critical value for instability predicted by elastic analysis, may not
349 facilitate stick-slip instability if the yield strength is low enough. Since stiffness is inversely
350 proportional to length, this finding suggests that not all perturbations with wavelength greater than
351 the nucleation length are unstable. Rather the maximum wavelength that is unstable may vary
352 depending on yield strength. This implies, for some parameter regime in the presence of off-fault
353 plasticity, that only partial ruptures may exist and that these ruptures cannot grow to become fault
354 spanning events. Similar patterns are observed in continuum 2D anti-plane simulations with
355 different values of yield strength. The rich slip patterns observed in the continuum model include
356 locked fault, slow slip events, localized sequence of seismic event and irregular patterns with
357 partial ruptures spreading over the fault. Neither frictional heterogeneity nor pore pressure
358 perturbation is introduced here. Only the bulk strength is acting as the controlling factor in
359 modulating the slip pattern.

360 In a characteristic seismic cycle, VS patch accumulates slip during the interseismic period and VW
361 patch catches up with seismic slip accumulation. However, when the bulk strength is relatively
362 low, seismic events are rare or spatially limited with partial ruptures. This results in slip deficit
363 prevailing throughout the seismic cycle. We found that off-fault plastic deformation compensates
364 for the slip deficit in this case. For sufficiently low bulk strength, fault may remain locked without
365 generating seismic events while off-fault bulk accommodates the deformation through plastic
366 deformation. This is also analogous to the spring slider results where plastic deformation in the
367 spring resists and even, in some cases, prevents the sliding of the block. Relative amount of off-
368 fault plastic deformation and on-fault slip is associated with the spectrum of slip from clustered

369 fast slip to a mixture of fast and slow slip as the yield strength decreases. Inelastic dissipation must
370 remain low for fast fault large events to exist.

371 We note that large amount of shallow off-fault deformation, exceeding 80% of the total surface
372 deformation (i.e., 4 times the on-fault slip) has been reported around some faults recently by Li et
373 al., (2022). They hypothesized that the large amount of off-fault deformation may include some
374 elastic deformation. The determination of the extent of inelastic off-fault deformation would be
375 possible if additional data from seismic reflection was available. The plastic strain in our
376 simulation is limited to a narrow region close to the fault (Supplementary Figure-S4). If this holds
377 true for off-fault plasticity accumulation in natural fault zones, particularly at depth, it may be
378 difficult to distinguish between on-fault and off-fault deformation from field observations specially
379 from satellite measurements as there are limitations on high resolution measurements of off-fault
380 deformation (Antoine et al., 2021). This partitioning of deformation is, however, important to
381 quantify as accumulation of off-fault plasticity may have implications for fault weakening. As
382 plastic deformation involves dissipation over narrow but finite region, it can influence the heat
383 diffusion and constrain the rise of temperature associated with slip localization into an extremely
384 thin surface in an otherwise elastic medium (Rice 2006). This may contribute to understanding the
385 scarcity of fault zone melting in some field observations. However, since most of the plastic
386 dissipation is still in the form of heat, we do not think that off-fault plasticity resolves the heat flow
387 anomaly.

388 Slow slip events recorded in some field observations show a wide range of durations in the scale
389 of days to months, and large earthquakes have been found after the migration of slow slip events
390 and small earthquakes (Ito et al., 2013; Ruiz et. al., 2014; Obara & Kato, 2016). The coexistence
391 of slow slip events and small earthquakes in subduction zone has also been reported by Ito et al.,

392 2007. In our simulation, fault slip accompanied by a mixture of seismic events with partial ruptures
393 and slow slip events are observed. Some of the slow slip events show spatial migration over the
394 seismogenic patch with duration reaching the scale of months. We observe emergence of spectrum
395 of slip by simulating different cases with small difference in yield strength. In natural fault zone,
396 off-fault bulk property (for example, yield strength) may vary spatially and evolve with time. Since
397 yield strength depends on effective normal stress, physical process like fluid pressure perturbation
398 may alter the yield strength independent of fault strength alteration depending on the hydraulic
399 properties in the fault core relative to the fault zone. Healing of damaged fault zone may also
400 contribute to the evolution of yield strength. Consequently, a fault may host different patterns of
401 slip switching from fast seismic rupture to slow aseismic slip when yield strength transiently
402 decreases.

403 The localized seismic events observed in our continuum simulations, at the boundary of the VW
404 and VS regions, is analogous to repeating microseismicity model presented in Sammis & Rice
405 (2000) but some differences exist. The similarity is that the location of the seismic events is near
406 the transition between creeping asperity (VS patch) and seismogenic locked asperity (VW patch).
407 The slip deficit in their model is compensated by occasional full-fault spanning events whereas the
408 slip deficit in our simulations is compensated by off-fault plastic deformation. Also, in our
409 simulations, there are slow slip events in between the seismic events.

410 Numerical modeling of fault damage zone (Nie & Barbot 2022; Thakur & Huang, 2021;
411 Abdelmeguid et al., 2019; Kaneko et al., 2011) with a layer of reduced elastic modulus shows
412 increased slip rate, and a range of slip pattern depending on the width and the contrast of elastic
413 modulus. A more compliant layer near the fault corresponds to generate more intense rupture. On
414 the other hand, plasticity as a dissipative mechanism influences the rupture characteristics resulting

415 in reduced slip rate and rupture speed (Templeton & Rice, 2008; Viesca et al., 2008; Dunham et
416 al. 2011a, 2011b; Gabriel et al., 2013). Furthermore, in contrast to elastic bulk, plasticity limits the
417 stress concentration ahead of the rupture tip. It acts as a barrier to rupture propagation and may
418 result in spatial segmentation and temporal clustering (Mia et al., 2022). In this study, we model
419 elastoplastic deformation of off-fault bulk keeping the elastic modulus constant throughout. Total
420 deformation is partitioned into fault slip and off-fault plastic deformation. Depending on the bulk
421 yield strength and frictional strength, the contribution of plasticity may compensate for a larger
422 amount of the total deformation and reduce fault slip leading to emergence of a variety of slip
423 patterns from fast to slow. However, fault zone inelasticity may include processes that go beyond
424 plastic dissipation such as co-seismic degradation of the elastic moduli and their inter-seismic
425 healing. The time-dependent modulation of the fault zone elastic properties may further enrich the
426 observed slip complexity, enhance seismic radiation, and expand the conditions for generation of
427 slow slip. Incorporation of off-fault plasticity coupled with damage rheology in SEAS is a focus
428 of a future investigation.

429 In this model, we consider the frictional parameters like reference friction coefficient, direct effect,
430 and state evolution coefficient to remain stationary. However, frictional parameters may evolve
431 with coseismic deformation (Kaproth & Marone, 2013; Im et al., 2020) which may get pronounced
432 with off-fault damage or plasticity accumulation. Investigating the interplay between evolving
433 fault friction as well as degradation and subsequent healing of fault zone material warrants future
434 study. Fault zone geometric complexity including nonplanar faults, and interaction of multiple
435 faults in presence of off-fault material non-linearity, is planned as future study. Furthermore,
436 evolution of pore pressure associated with volumetric deformation of the fault zone needs to be

437 considered for its vast implications on the evolution of strength and deformation in fluid-saturated
438 fault zones.

439 **Acknowledgement**

440 The authors acknowledge support from the Southern California Earthquake Center through a
441 collaborative agreement between NSF. Grant Number: EAR0529922 and USGS. Grant Number:
442 07HQAG0008 and the National Science Foundation CAREER award No. 1753249 for modeling
443 complex fault zone structures. This material is also based upon work partially supported by the
444 Department of Energy under Award Number DE-FE0031685 to investigate spatio-temporal
445 complexity of induced earthquakes. The authors are also grateful for the insightful comments from
446 two anonymous reviewers, which helped improve the manuscript.

447 **Data Availability Statement**

448 The authors accept the data policy. Data generated from the numerical simulations are uploaded
449 on an open access repository (10.5281/zenodo.7718768).

450 **References**

- 451 Abdelmeguid, M., Ma, X., & Elbanna, A. (2019). A Novel Hybrid Finite Element-Spectral Boundary
452 Integral Scheme for Modeling Earthquake Cycles: Application to Rate and State Faults With Low-
453 Velocity Zones. *Journal of Geophysical Research: Solid Earth*, 124(12), 12854–12881.
454 <https://doi.org/10.1029/2019JB018036>
- 455 Abdelmeguid, M., & Elbanna, A. (2022a). Sequences of seismic and aseismic slip on bimaterial faults show
456 dominant rupture asymmetry and potential for elevated seismic hazard. *Earth and Planetary Science*
457 *Letters*, 593. <https://doi.org/10.1016/j.epsl.2022.117648>
- 458 Abdelmeguid, M., & Elbanna, A. (2022b). Modeling Sequences of Earthquakes and Aseismic Slip (SEAS)
459 in Elasto-Plastic Fault Zones With a Hybrid Finite Element Spectral Boundary Integral Scheme. *Journal of*
460 *Geophysical Research: Solid Earth*, 127(12). <https://doi.org/10.1029/2022JB024548>
- 461 Allison, K. L., & Dunham, E. M. (2021). Influence of Shear Heating and Thermomechanical Coupling on
462 Earthquake Sequences and the Brittle-Ductile Transition. *Journal of Geophysical Research: Solid*
463 *Earth*, 126(6). <https://doi.org/10.1029/2020JB021394>

- 464 Ampuero, J. P., & Rubin, A. M. (2008). Earthquake nucleation on rate and state faults - Aging and slip
465 laws. *Journal of Geophysical Research: Solid Earth*, 113(1). <https://doi.org/10.1029/2007JB005082>
- 466 Antoine, S. L., Klinger, Y., Delorme, A., Wang, K., Bürgmann, R., & Gold, R. D. (2021). Diffuse
467 deformation and surface faulting distribution from submetric image correlation along the 2019
468 Ridgecrest, California, ruptures. *Bulletin of the Seismological Society of America*, 111(5), 2275-2302.
469 <https://doi.org/10.1785/0120210036>
- 470 Avouac, J. P. (2015). From geodetic imaging of seismic and aseismic fault slip to dynamic modeling of the
471 seismic cycle. *Annual Review of Earth and Planetary Sciences*, 43, 233–271.
472 <https://doi.org/10.1146/annurev-earth-060614-105302>
- 473 Barbot, S., Lapusta, N., & Avouac, J.-P. (2012). Under the Hood of the Earthquake Machine: Toward
474 Predictive Modeling of the Seismic Cycle. *Science*, 336(6082), 707–710.
475 <https://doi.org/10.1126/science.1218796>
- 476 Barbot, S. (2019). Slow-slip, slow earthquakes, period-two cycles, full and partial ruptures, and
477 deterministic chaos in a single asperity fault. *Tectonophysics*, 768.
478 <https://doi.org/10.1016/j.tecto.2019.228171>
- 479 Bedford, J. D., Faulkner, D. R., & Lapusta, N. (2022). Fault rock heterogeneity can produce fault weakness
480 and reduce fault stability. *Nature Communications*, 13(1). <https://doi.org/10.1038/s41467-022-27998-2>
- 481 Ben-Zion, Y., & Rice, J. R. (1997). Dynamic simulations of slip on a smooth fault in an elastic
482 solid. *Journal of Geophysical Research: Solid Earth*, 102(B8), 17771-17784.
- 483 Ben-Zion, Y., & Rice, J. R. (1993). Earthquake failure sequences along a cellular fault zone in a three-
484 dimensional elastic solid containing asperity and nonasperity regions. *Journal of Geophysical
485 Research*, 98(B8). <https://doi.org/10.1029/93jb01096>
- 486 Ben-Zion, Y., & Sammis, C. G. (2003). Characterization of Fault Zones. In *Pure appl. geophys* (Vol. 160).
- 487 Beroza, G. C., & Ide, S. (2011). Slow earthquakes and nonvolcanic tremor. *Annual Review of Earth and
488 Planetary Sciences*, 39, 271–296. <https://doi.org/10.1146/annurev-earth-040809-152531>
- 489 Bürgmann, R. (2018). The geophysics, geology and mechanics of slow fault slip. *Earth and Planetary
490 Science Letters*, 495, 112–134. <https://doi.org/10.1016/j.epsl.2018.04.062>
- 491 Cattania, C. (2019). Complex Earthquake Sequences On Simple Faults. *Geophysical Research Letters*,
492 46(17–18), 10384–10393. <https://doi.org/10.1029/2019GL083628>
- 493 Chen, T., & Lapusta, N. (2009). Scaling of small repeating earthquakes explained by interaction of seismic
494 and aseismic slip in a rate and state fault model. *J. Geophys. Res.*, 114, 1311.
495 <https://doi.org/10.1029/2008JB005749>
- 496 Chen, Y., Liu, M., & Luo, G. (2020). Complex temporal patterns of large earthquakes: Devil's staircases.
497 *Bulletin of the Seismological Society of America*, 110(3), 1064–1076.
498 <https://doi.org/10.1785/0120190148>
- 499 Collettini, C., Barchi, M. R., de Paola, N., Trippetta, F., & Tinti, E. (2022). Rock and fault rheology explain
500 differences between on fault and distributed seismicity. *Nature Communications*, 13(1).
501 <https://doi.org/10.1038/s41467-022-33373-y>
- 502 Collettini, C., Tesei, T., Scuderi, M. M., Carpenter, B. M., & Viti, C. (2019). Beyond Byerlee friction, weak
503 faults and implications for slip behavior. *Earth and Planetary Science Letters*, 519, 245-263.
504 <https://doi.org/10.1016/j.epsl.2019.05.011>

505 Dieterich, J. H. (1978). Time-dependent friction and the mechanics of stick-slip. *Pure and Applied*
506 *Geophysics PAGEOPH*, 116(4-5), 790-806.

507 Dieterich, J. H. (1979). Modeling of rock friction: 1. Experimental results and constitutive
508 equations. *Journal of Geophysical Research: Solid Earth*, 84(B5), 2161-2168.

509

510 Dragert, H., Wang, K., & James, T. S. (2001). A Silent Slip Event on the Deeper Cascadia Subduction
511 Interface. *Science*, 292(5521), 1525–1528. <https://doi.org/10.1126/science.1060152>

512 Dunham, E. M., Belanger, D., Cong, L., & Kozdon, J. E. (2011). Earthquake ruptures with strongly rate-
513 weakening friction and off-fault plasticity, Part 1: Planar faults. *Bulletin of the Seismological Society*
514 *of America*, 101(5), 2296-2307.

515 Dunham, E. M., Belanger, D., Cong, L., & Kozdon, J. E. (2011). Earthquake ruptures with strongly rate-
516 weakening friction and off-fault plasticity, Part 2: Nonplanar faults. *Bulletin of the Seismological*
517 *Society of America*, 101(5), 2308-2322.

518 Erickson, B. A., Dunham, E. M., & Khosravifar, A. (2017). A finite difference method for off-fault
519 plasticity throughout the earthquake cycle. *Journal of the Mechanics and Physics of Solids*, 109, 50-77.

520 Erickson, B. A., Jiang, J., Lambert, V., Barbot, S. D., Abdelmeguid, M., Almquist, M., Ampuero, J.-P.,
521 Ando, R., Cattania, C., Chen, A., Dal Zilio, L., Deng, S., Dunham, E. M., Elbanna, A. E., Gabriel, A.-
522 A., Harvey, T. W., Huang, Y., Kaneko, Y., Kozdon, J. E., ... Yang, Y. (2023). Incorporating Full
523 Elastodynamic Effects and Dipping Fault Geometries in Community Code Verification Exercises for
524 Simulations of Earthquake Sequences and Aseismic Slip (SEAS). *Bulletin of the Seismological Society*
525 *of America*. <https://doi.org/10.1785/0120220066>

526 French, M. E., & Zhu, W. (2017). Slow fault propagation in serpentinite under conditions of high pore fluid
527 pressure. *Earth and Planetary Science Letters*, 473, 131-140.
528 <https://doi.org/10.1016/j.epsl.2017.06.009>

529 Fagereng, Å., & Sibson, R. H. (2010). Mélange rheology and seismic style. *Geology*, 38(8), 751-754.
530 <https://doi.org/10.1130/G30868.1>

531 Gabriel, A. A., Ampuero, J. P., Dalguer, L. A., & Mai, P. M. (2013). Source properties of dynamic rupture
532 pulses with off-fault plasticity. *Journal of Geophysical Research: Solid Earth*, 118(8), 4117-4126.

533 Goswami, A., & Barbot, S. (2018). Slow-slip events in semi-brittle serpentinite fault zones. *Scientific*
534 *Reports*, 8(1). <https://doi.org/10.1038/s41598-018-24637-z>

535 Heki, K., & Kataoka, T. (2008). On the biannually repeating slow-slip events at the Ryukyu Trench,
536 southwestern Japan. *Journal of Geophysical Research: Solid Earth*, 113(11).
537 <https://doi.org/10.1029/2008JB005739>

538 Im, K., Saffer, D., Marone, C., & Avouac, J. P. (2020). Slip-rate-dependent friction as a universal
539 mechanism for slow slip events. *Nature Geoscience*, 13(10), 705–710. [https://doi.org/10.1038/s41561-](https://doi.org/10.1038/s41561-020-0627-9)
540 [020-0627-9](https://doi.org/10.1038/s41561-020-0627-9)

541 Ito, Y., Hino, R., Kido, M., Fujimoto, H., Osada, Y., Inazu, D., Ohta, Y., Iinuma, T., Ohzono, M., Miura,
542 S., Mishina, M., Suzuki, K., Tsuji, T., & Ashi, J. (2013). Episodic slow slip events in the Japan
543 subduction zone before the 2011 Tohoku-Oki earthquake. *Tectonophysics*, 600, 14–26.
544 <https://doi.org/10.1016/j.tecto.2012.08.022>

- 545 Ito, Y., Obara, K., Shiomi, K., Sekine, S., & Hirose, H. (2007). Slow earthquakes coincident with episodic
546 tremors and slow slip events. *Science*, 315(5811), 503-506. <https://doi.org/10.1126/science.1134454>
- 547 Jiang, J., Erickson, B. A., Lambert, V. R., Ampuero, J. P., Ando, R., Barbot, S. D., Cattania, C., Zilio, L.
548 D., Duan, B., Dunham, E. M., Gabriel, A. A., Lapusta, N., Li, D., Li, M., Liu, D., Liu, Y., Ozawa, S.,
549 Pranger, C., & van Dinther, Y. (2022). Community-Driven Code Comparisons for Three-Dimensional
550 Dynamic Modeling of Sequences of Earthquakes and Aseismic Slip. *Journal of Geophysical Research:*
551 *Solid Earth*, 127(3). <https://doi.org/10.1029/2021JB023519>
- 552 Kaproth, B. M., & Marone, C. (2013). Slow Earthquakes, Preseismic Velocity Changes, and the Origin of
553 Slow Frictional Stick-Slip. *Science*, 341(6151), 1229–1232. <https://doi.org/10.1126/science.1239577>
- 554 Kaneko, Y., Avouac, J. P., & Lapusta, N. (2010). Towards inferring earthquake patterns from geodetic
555 observations of interseismic coupling. *Nature Geoscience*, 3(5), 363–369.
556 <https://doi.org/10.1038/ngeo843>
- 557 Kaneko, Y., Ampuero, J. P., & Lapusta, N. (2011). Spectral-element simulations of long-term fault slip:
558 Effect of low-rigidity layers on earthquake-cycle dynamics. *Journal of Geophysical Research: Solid*
559 *Earth*, 116(B10).
- 560 Lapusta, N., Rice, J. R., Ben-Zion, Y., & Zheng, G. (2000). Elastodynamic analysis for slow tectonic
561 loading with spontaneous rupture episodes on faults with rate- and state-dependent friction. *Journal of*
562 *Geophysical Research: Solid Earth*, 105(B10), 23765–23789. <https://doi.org/10.1029/2000jb900250>
- 563 Leeman, J. R., Saffer, D. M., Scuderi, M. M., & Marone, C. (2016). Laboratory observations of slow
564 earthquakes and the spectrum of tectonic fault slip modes. *Nature communications*, 7(1), 11104.
- 565 Lewis, M. A., & Ben-Zion, Y. (2010). Diversity of fault zone damage and trapping structures in the
566 Parkfield section of the San Andreas Fault from comprehensive analysis of near fault seismograms.
567 *Geophysical Journal International*, 183(3), 1579–1595. [https://doi.org/10.1111/j.1365-](https://doi.org/10.1111/j.1365-246X.2010.04816.x)
568 [246X.2010.04816.x](https://doi.org/10.1111/j.1365-246X.2010.04816.x)
- 569 Li, C., Li, T., Shan, X., & Zhang, G. (2022). Extremely Large Off-Fault Deformation during the 2021
570 Mw 7.4 Maduo, Tibetan Plateau, Earthquake. *Seismological Research Letters*.
571 <https://doi.org/10.1785/0220220139>
- 572 Liu, Y., & Rice, J. R. (2007). Spontaneous and triggered aseismic deformation transients in a subduction
573 fault model. *Journal of Geophysical Research: Solid Earth*, 112(9).
574 <https://doi.org/10.1029/2007JB004930>
- 575 Mia, M. S., Abdelmeguid, M., & Elbanna, A. E. (2022). Spatio-temporal clustering of seismicity enabled
576 by off-fault plasticity. *Geophysical Research Letters*, 49, e2021GL097601.
577 <https://doi.org/10.1029/2021GL097601>
- 578 Mitchell, T. M., & Faulkner, D. R. (2009). The nature and origin of off-fault damage surrounding strike-
579 slip fault zones with a wide range of displacements: A field study from the Atacama fault system,
580 northern Chile. *Journal of Structural Geology*, 31(8), 802–816.
581 <https://doi.org/10.1016/j.jsg.2009.05.002>
- 582 Miyake, Y., & Noda, H. (2019). Fully dynamic earthquake sequence simulation of a fault in a viscoelastic
583 medium using a spectral boundary integral equation method: does interseismic stress relaxation
584 promote aseismic transients?. *Earth, Planets and Space*, 71(1), 1-12.
- 585 Nie, S., & Barbot, S. (2022). Rupture styles linked to recurrence patterns in seismic cycles with a compliant
586 fault zone. *Earth and Planetary Science Letters*, 591. <https://doi.org/10.1016/j.epsl.2022.117593>

587 Nakata, R., Ando, R., Hori, T., & Ide, S. (2011). Generation mechanism of slow earthquakes: Numerical
588 analysis based on a dynamic model with brittle-ductile mixed fault heterogeneity. *Journal of*
589 *Geophysical Research: Solid Earth*, 116(8). <https://doi.org/10.1029/2010JB008188>

590 Noda, H., & Lapusta, N. (2013). Stable creeping fault segments can become destructive as a result of
591 dynamic weakening. *Nature*, 493(7433), 518–521. <https://doi.org/10.1038/nature11703>

592 Obara, K., & Kato, A. (2016). Connecting slow earthquakes to huge earthquakes. *Science*, 353(6296), 253-
593 257. <https://doi.org/10.1126/science.aaf1512>

594 Radiguet, M., Cotton, F., Vergnolle, M., Campillo, M., Walpersdorf, A., Cotte, N., & Kostoglodov, V.
595 (2012). Slow slip events and strain accumulation in the Guerrero gap, Mexico. *Journal of Geophysical*
596 *Research: Solid Earth*, 117(4). <https://doi.org/10.1029/2011JB008801>

597 Ranjith, K., & Rice, J. R. (1999). Stability of quasi-static slip in a single degree of freedom elastic system
598 with rate and state dependent friction. *Journal of the Mechanics and Physics of Solids*, 47(6), 1207-
599 1218. [https://doi.org/10.1016/S0022-5096\(98\)00113-6](https://doi.org/10.1016/S0022-5096(98)00113-6)

600 Rice, J. R. (2006). Heating and weakening of faults during earthquake slip. *Journal of Geophysical*
601 *Research: Solid Earth*, 111(5). <https://doi.org/10.1029/2005JB004006>

602 Rice, J. R., & Ruina, A. L. (1983). Stability of Steady Frictional Slipping. In *Journal of Applied*
603 *Mechanics*, 50(2), 343-349. <https://doi.org/10.1115/1.3167042>

604 Rice, J. R., Lapusta, N., & Ranjith, K. (2001). Rate and state dependent friction and the stability of sliding
605 between elastically deformable solids. *Journal of the Mechanics and Physics of Solids*, 49(9), 1865-
606 1898. [https://doi.org/10.1016/S0022-5096\(01\)00042-4](https://doi.org/10.1016/S0022-5096(01)00042-4)

607 Ross, Z. E., Cochran, E. S., Trugman, D. T., &
608 Smith, J. D. (2020). 3D fault architecture controls the dynamism of earthquake swarms. *Science*,
368(6497), 1357–1361. <https://doi.org/10.1126/science.abb0779>

609 Ruina, A. (1983). Slip instability and state variable friction laws. *Journal of Geophysical Research: Solid*
610 *Earth*, 88(B12), 10359-10370.

611 Ruiz, S., Metois, M., Fuenzalida, A., Ruiz, J., Leyton, F., Grandin, R.,
612 ... & Campos, J. (2014). Intense foreshocks and a slow slip event preceded the 2014 Iquique M w 8.1
earthquake. *Science*, 345(6201), 1165-1169. <https://doi.org/10.1126/science.1256074>

613 Sammis, C. G., & Rice, J. R. (2001). Repeating Earthquakes as Low-Stress-Drop Events at a Border
614 between Locked and Creeping Fault Patches. *Bulletin of the Seismological Society of America*, 91(3),
615 532-537. <https://doi.org/10.1785/0120000075>

616 Scuderi, M. M., Marone, C., Tinti, E., Di Stefano, G., & Collettini, C. (2016). Precursory changes in seismic
617 velocity for the spectrum of earthquake failure modes. *Nature geoscience*, 9(9), 695-700.
618 <https://doi.org/10.1038/ngeo2775>

619 Segall, P., Rubin, A. M., Bradley, A. M., & Rice, J. R. (2010). Dilatant strengthening as a mechanism for
620 slow slip events. *Journal of Geophysical Research: Solid Earth*, 115(12).
621 <https://doi.org/10.1029/2010JB007449>

622 Skarbak, R. M., Rempel, A. W., & Schmidt, D. A. (2012). Geologic heterogeneity can produce aseismic
623 slip transients. *Geophysical Research Letters*, 39(21). <https://doi.org/10.1029/2012GL053762>

624 Templeton, E. L., & Rice, J. R. (2008). Off-fault plasticity and earthquake rupture dynamics: 1. Dry
625 materials or neglect of fluid pressure changes. *Journal of Geophysical Research: Solid Earth*, 113(B9).

626 Thakur, P., Huang, Y., & Kaneko, Y. (2020). Effects of low-velocity fault damage zones on long-term
627 earthquake behaviors on mature strike-slip faults. *Journal of Geophysical Research: Solid*
628 *Earth*, 125(8), e2020JB019587.

- 629 Thakur, P., & Huang, Y. (2021). Influence of fault zone maturity on fully dynamic earthquake
630 cycles. *Geophysical Research Letters*, 48(17), e2021GL094679.
- 631 Tong, X., & Lavier, L. L. (2018). Simulation of slip transients and earthquakes in finite thickness shear
632 zones with a plastic formulation. *Nature Communications*, 9(1). [https://doi.org/10.1038/s41467-018-](https://doi.org/10.1038/s41467-018-06390-z)
633 [06390-z](https://doi.org/10.1038/s41467-018-06390-z)
- 634 Viesca, R. C., Templeton, E. L., & Rice, J. R. (2008). Off-fault plasticity and earthquake rupture dynamics:
635 2. Effects of fluid saturation. *Journal of Geophysical Research: Solid Earth*, 113(B9).
- 636 Wu, B. (2021). *Explaining Slow Earthquake Phenomena with a Frictional-Viscous Faulting*
637 *Model* (Doctoral dissertation, University of California, Riverside).

Supplementary Information for

The Spectrum of Fault Slip in Elastoplastic Fault Zones

Md Shumon Mia^{1,2}, Mohamed Abdelmeguid^{2,3}, Ahmed E. Elbanna^{2,4}

¹Department of Mechanical Science and Engineering, University of Illinois at Urbana-Champaign, Urbana, IL, USA.

²Department of Civil and Environmental Engineering, University of Illinois at Urbana-Champaign, Urbana, IL, USA.

³Graduate Aerospace Laboratories, California Institute of Technology, Pasadena, CA, USA.

⁴Beckman Institute of Advanced Science and Technology, University of Illinois at Urbana-Champaign, Urbana, IL, USA.

Corresponding author: Md Shumon Mia (mmia2@illinois.edu)

Contents of this file

Text S1 to S3

Tables S1

Figures S1 to S4

Introduction

The Supplementary Information includes:

- Text S1 outlines the frictional law.
- Text S2 outlines the elastoplastic spring slider model.
- Text S3 outlines the model setup and methods.
- Table S1 provides input parameters for the simulations.
- Figure S1 shows schematic of fault zone and elastoplastic spring slider model.
- Figure S2 shows model geometry and hybrid scheme setup.
- Figure S3 shows results of fully dynamics simulations for yield strength 33.5 MPa, 36 MPa and elastic case. Slip patterns are qualitatively similar to the quasi-dynamics cases presented in the main text.
- Figure S4 shows spatial extent of off-fault plasticity for yield strength 31 MPa and 33.5 MPa.

Text S1. Rate-and-state friction

The fault friction is governed by a regularized rate-and-state friction law (Dieterich, 1979; Ruina, 1983; Ben-Zion & Rice, 1997; Lapusta et al., 2000) where the friction coefficient, f , is a function of slip rate, V , and state variable, θ .

$$f(V, \theta) = a \sinh^{-1} \left[\frac{V}{2V_0} \exp \left(\frac{f_0 + b \ln(V_0 \theta / L)}{a} \right) \right] \quad (\text{Eqn-1.1}).$$

Here, a and b are non-negative dimensionless frictional parameters related to direct effect and state evolution respectively. $a < b$ indicates velocity weakening friction whereas $a > b$ indicates velocity strengthening friction. f_0 is the reference friction coefficient with a reference slip rate V_0 . L is characteristic slip distance. State variable, θ , refers to the time of contact between the sliding asperities which evolves following a prescribed aging law (Dieterich, 1978; Ruina, 1983; Ben-Zion & Rice, 1997; Ampuero & Rubin, 2008):

$$\frac{d\theta}{dt} = 1 - \frac{V\theta}{L} \quad (\text{Eqn-1.2}).$$

For constant normal stress, σ_n , fault strength is then expressed as $\sigma_n f(V, \theta)$. In case of pore pressure perturbation $P(x, t)$, effective normal stress is $\sigma_e(x, t) = \sigma_n - P(x, t)$, and fault strength becomes $\sigma_e(x, t) f(V, \theta)$. We model dry case considering no perturbation of pore pressure i.e., $\sigma_e(x, t) = \sigma_n$. Approximating inertia with radiation damping, called quasi-dynamics approach (Rice 1993; Ranjith & Rice, 1999), shear stress in the frictional interface is given by,

$$\tau = \sigma_e f(V, \theta) + \eta_r V \quad (\text{Eqn-1.3}).$$

Here, the radiation damping coefficient is given by $\eta_r = \frac{\mu}{2c_s}$.

Text S2. Elastoplastic spring slider model

We model a spring-block system sliding on a frictional interface as shown in Figure-S1. Here we consider a simplified representation of a planar fault surface with uniform friction and elastoplastic fault zone. We use the rate-and-state friction law described in the previous section. The frictional interface is velocity weakening which means steady state friction coefficient decreases with the increase in slip rate. The spring with stiffness (k) and yield strength (σ_y) idealize the bulk material with elastoplastic response. A constant load point velocity (V_p) is applied at the end of the spring representing the background tectonic plate rate.

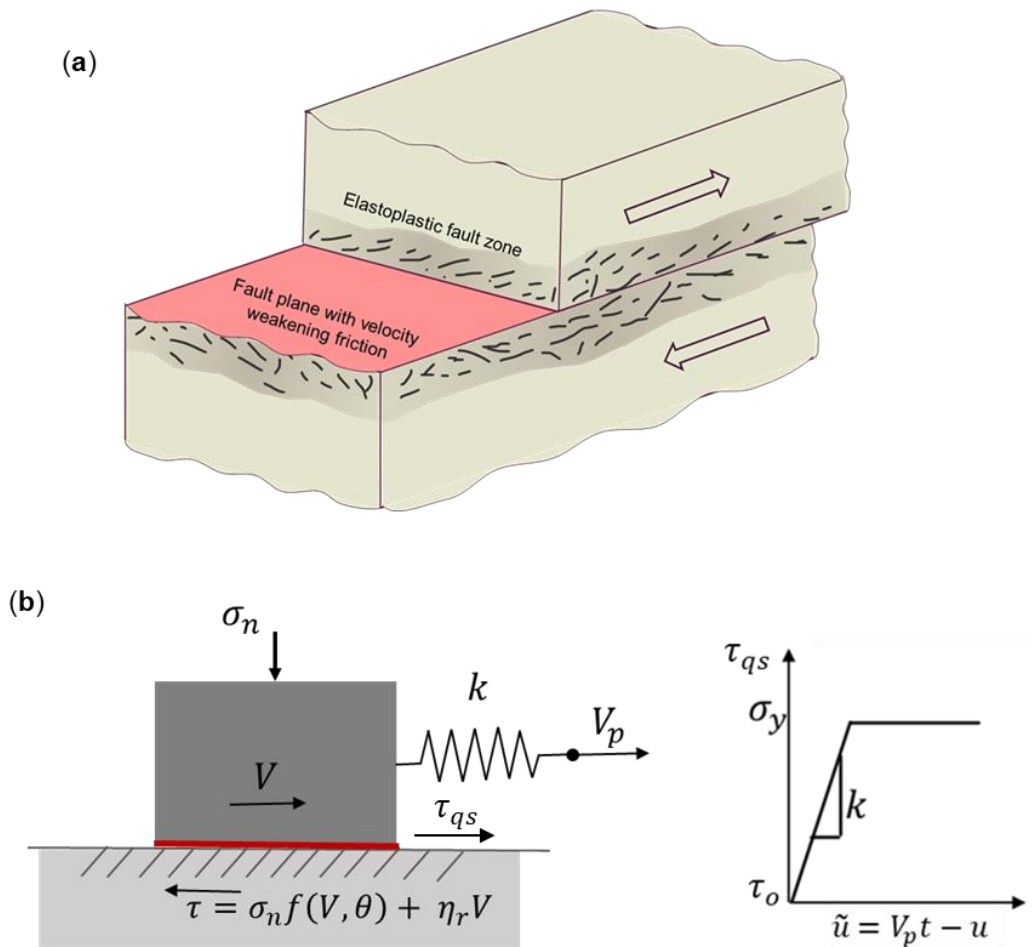


Figure S1. A schematic of the fault zone and spring slider model with rate-and-state frictional interface. (a) Schematic of elastoplastic fault zone and simplified planar fault surface with uniform velocity weakening friction. (b) Elastoplastic spring slider model where constant driving velocity (V_p) is applied at the load point of the spring and other end is attached to a slider. V is the slider velocity (slip rate), and u is the slider displacement (slip). Spring response is elastic perfectly plastic. k is the spring stiffness per unit frictional contact and σ_y is the yield strength. Frictional stress (τ) balances the stress from the spring (τ_{qs}).

Inertia is approximated with radiation damping which leads to the frictional stress opposing the motion expressed as

$$\tau = \sigma_n f(V, \theta) + \eta_r V \quad (\text{Eqn-2.1}).$$

σ_n is the normal stress, $f(V, \theta)$ is the friction coefficient governed by rate-and-state friction law as a function of slip rate V and state variable θ . Radiation damping coefficient is given by $\eta_r = \frac{\mu}{2c_s}$. Where μ is shear modulus of the bulk and c_s is the shear wave speed.

Here, the interfacial slip is equal to the total block displacement. For a total block displacement u , the total extension of the spring at time t is given by $\tilde{u} = V_p t - u$. For the case of an elastoplastic spring, this total extension is the summation of elastic and plastic deformation, $\tilde{u} = \tilde{u}^e + \tilde{u}^p$. Spring force is proportional to its elastic deformation. Considering k as the stiffness for unit area of frictional interface leads to a stress from the deformation of spring at time t given by,

$$\tau_{qs} = \tau_o + k(V_p t - u - \tilde{u}^p) \quad (\text{Eqn-2.2}).$$

τ_o is initial stress which satisfies friction law with initial slip rate and state variable. For plastic deformation, this stress is bounded by the yield strength (σ_y) defining the yield surface in 1D plasticity model with no hardening,

$$|\tau_{qs}| \leq \sigma_y \quad (\text{Eqn-2.3})$$

The rate of plastic deformation given by the flow rule expressed as,

$$\dot{\tilde{u}}^p = \dot{\gamma} \text{sign}(\tau_{qs}) \quad (\text{Eqn-2.4}).$$

$\dot{\gamma}$ is the magnitude of the rate of plastic deformation.

The frictional stress is equal to the stress due to the deformation of spring which leads to

$$\tau_{qs} = \sigma_n f(V, \theta) + \eta_r V \quad (\text{Eqn-2.5}).$$

Slip rate (V) is computed from the above equation, and integration of slip rate gives the slip which is the slider displacement (u). State variable evolution follows aging law,

$$\dot{\theta} = 1 - V\theta/L \quad (\text{Eqn-2.6}).$$

L is the characteristic slip distance.

Solution steps:

At any time, t , for given $\theta(t)$, $u(t)$ we use return mapping algorithm (Simo & Hughes, 2006; Abdelmeguid & Elbanna, 2022b) to march in time from $t_n = t$ to $t_{n+1} = t + \Delta t$.

1. Compute elastic trial stress, $\tau_{qs_{n+1}}^{trial} = \tau_o + k(V_p t_{n+1} - u_n - \tilde{u}_n^p)$
2. Check for plasticity:

$$\text{If } |\tau_{qs_{n+1}}^{trial}| < \sigma_y$$

$$\tau_{qs_{n+1}} = \tau_{qs_{n+1}}^{trial} \text{ (Elastic)}$$

$$\Delta \tilde{u}^p = 0$$

Otherwise, plastic deformation with

$$\tau_{qs_{n+1}} = \sigma_y$$

$$\Delta \tilde{u}^p = \frac{|\tau_{qs_{n+1}}^{trial}| - \sigma_y}{k} \text{sign}(\tau_{qs_{n+1}}^{trial})$$

$$\tilde{u}_{n+1}^p = \tilde{u}_n^p + \Delta \tilde{u}^p$$

3. Compute slip rate (V) equating τ_{qs} with frictional stress, $\tau_{qs} = \sigma_n f(V, \theta) + \eta_r V$
4. Compute slider displacement, $u(t + \Delta t) = u(t) + V \Delta t$
5. Update state variable, $\theta(t + \Delta t) = \theta(t) + \dot{\theta} \Delta t$
6. Estimate time increment based on slip rate and characteristic slip distance (L) criteria, $\Delta t = \min [C \frac{L}{V}]$ as described in Lapusta et al. (2000).

Text S3. Model Setup and Methods

The model includes frictional interface (fault) embedded in a 2D whole space (Figure-S1).

Balance of linear momentum leads to the equilibrium equation:

$$\sigma_{ij,j} + b_i = \rho \ddot{u}_i \text{ in } \Omega \quad (\text{Eqn-3.1}).$$

For 2D anti-plane deformation, displacement at any point (x, y) , and time t , is $u_z(x, y, t)$.

Corresponding stress components are σ_{xz} and σ_{yz} . Eqn-3.1 gives wave equation for linear elastic homogeneous material with infinitesimal strain approximation. Slow deformation during interseismic period allows ignoring inertia term and solving a series of static equilibria with tectonic plate deformation and friction boundary condition on the fault surface. Ignoring body force (b_i) and dropping inertia term ($\rho \ddot{u}_i$) Eqn-3.1 reduces to

$$\frac{\partial \sigma_{xz}}{\partial x} + \frac{\partial \sigma_{yz}}{\partial y} = 0 \quad (\text{Eqn-3.2}).$$

Slip constraint on the frictional interface at $y = 0$ is given by,

$$u_z(x, 0^+, t) - u_z(x, 0^-, t) = d(x, t) \quad (\text{Eqn-3.3}).$$

Continuity of traction across the fault plane leads to

$$\sigma_{yz}(x, 0^+, t) = \sigma_{yz}(x, 0^-, t) = T^f \quad (\text{Eqn-3.4}).$$

For elastoplastic bulk, constitutive relation with additive decomposition of total strain gives

$$\dot{\sigma}_{xz} = 2\mu (\dot{\epsilon}_{xz} - \dot{\epsilon}_{xz}^p), \text{ and } \dot{\sigma}_{yz} = 2\mu (\dot{\epsilon}_{yz} - \dot{\epsilon}_{yz}^p) \quad (\text{Eqn-3.5}).$$

Here, μ is the shear modulus and components of the symmetric total strain tensor are given by,

$$\epsilon_{xz} = \frac{1}{2} \frac{\partial u_z}{\partial x}, \text{ and } \epsilon_{yz} = \frac{1}{2} \frac{\partial u_z}{\partial y} \quad (\text{Eqn-3.6}).$$

We use the J2 plasticity model to capture the inelastic response of the off-fault bulk. For 2D anti-plane problem, it reduces to a yield function:

$$F(\sigma) = \sqrt{(\sigma_{xz}^2 + \sigma_{yz}^2)} - \sigma_y \quad (\text{Eqn-3.7}).$$

σ_y is the bulk yield strength. Plastic strain rate is expressed as,

$$\dot{\epsilon}_{xz}^p = \dot{\gamma} \frac{\partial F}{\partial \sigma_{xz}}, \quad \text{and} \quad \dot{\epsilon}_{yz}^p = \dot{\gamma} \frac{\partial F}{\partial \sigma_{yz}} \quad (\text{Eqn-3.8}).$$

$\dot{\gamma}$ is the consistency parameter defining the rate of equivalent plastic strain. We use a radial return mapping algorithm (Simo & Hughes, 2006; Abdelmeguid & Elbanna, 2022b) to update the stresses.

In earthquake cycle simulation, the above equations need to be solved for an effectively unbounded domain. Spectral boundary integral enables truncating the computational domain by replacing the exterior homogeneous linear elastic half spaces with integral relation between the shear stress and displacement history (Breitenfeld & Geubelle, 1998; Geubelle & Breitenfeld, 1997; Geubelle & Rice, 1995; Lapusta et al., 2000; Abdelmeguid et al., 2019; Abdelmeguid & Elbanna 2022a, 2022b). For 2D antiplane problem, the shear stress at the boundary of the homogeneous half space is given by

$$T_3^{s\pm}(x, t) = T_3^o{}^{s\pm}(x, t) \mp \frac{\mu}{c_s} \dot{u}_3^\pm(x, t) + f_3^\pm(x, t) \quad (\text{Eqn-3.9}).$$

The superscripts +, and - indicate top and bottom half space respectively. T_3^o represents the initial stress as well as any externally applied stress. \dot{u}_3 represent particle velocity and c_s is shear wave speed. f_3 is a functional resulting from space-time convolution of the displacement history at the boundary expressed in Fourier domain. In the velocity representation, the Fourier coefficient of $f_3^\pm(x, t)$ is expressed as

$$F_3^\pm(t; k_n) = \mp \mu |k_n| U_3^\pm(t; k_n) \pm \int_0^t W_{33}(|k_n| c_s t') \dot{U}_3^\pm(t - t'; k_n) dt' \quad (\text{Eqn-3.10}).$$

The convolution kernel is given by $W_{33}(\xi) = \int_{\xi}^{\infty} \frac{J_1(\zeta)}{\zeta} d\zeta$, where $J_1(\zeta)$ is the order one Bessel function of the first kind. Wave number, $k_n = 2\pi n/\lambda$, with replication length λ . U_3 and \dot{U}_3 are the Fourier coefficients of displacement and velocity respectively. For the aseismic slow deformation phase, the velocity terms from Eqn-3.9 and Eqn-3.10 can be neglected. The first term in Eqn-3.10 represents the static contribution,

$$\tilde{F}_3^{\pm}(t; k_n) = \mp \mu |k_n| U_3^{\pm}(t; k_n) \quad (\text{Eqn-3.11}).$$

Also considering the stress increment beyond the initial condition, we can set $T_3^{s\pm} = 0$. Therefore, the boundary stress, $T_3^{s\pm}(x, t)$ can be calculated using inverse Fourier transform of $\tilde{F}_3^{\pm}(t; k_n)$.

We incorporate the fault surface in FEM using domain decomposition technique (Aagaard et al., 2013), where the Lagrange multiplier represents fault traction (T^f). Weak form of the governing equation gives following system of equations (Abdelmeguid et al., 2019; Abdelmeguid & Elbanna, 2022b):

$$\mathbf{K}u - F^p + \mathbf{L}_f^T T^f + \mathbf{L}_s^T T^s = F \quad (\text{Eqn-3.12})$$

$$\mathbf{L}_f u = \mathbf{L}_d d \quad (\text{Eqn-3.13}).$$

For elastoplastic bulk, plastic force is obtained by integrating the plastic strain, $F^p = \int_{\Omega} \mathbf{B}^T \mathbf{D} \epsilon^p d\Omega$. Where, \mathbf{B} is the strain-displacement matrix, \mathbf{D} is the matrix with material moduli. \mathbf{K} denotes the stiffness matrix; F is the force vector. \mathbf{L}_f , \mathbf{L}_d and \mathbf{L}_s is comes from integrating the shape function.

We use a predictor-corrector approach to solve for the unknown displacements and fault tractions. Fault slip rate is then calculated from the following equation by equating fault

total traction with fault strength and including radiation damping approximation for inertia (called quasi-dynamics approach). With radiation damping coefficient, $\eta_r = \frac{\mu}{2c_s}$,

$$T^f + T_o^f = \sigma_e f(V, \theta) + \frac{\mu V}{2c_s} \quad (\text{Eqn-3.14}).$$

T_o^f is fault initial traction. Slip for next time step is computed by integrating the slip rate.

Solution steps for Quasi-dynamics solver:

1. At any time, t , for given slip, $d(t)$, state variable, $\theta(t)$, applied tectonic deformation, $u_b(t) = V_p t$, displacement $u(t - \Delta t)$, plastic strain, $\epsilon^p(t - \Delta t)$ and hence plastic force, $F^p(t - \Delta t) = \int_{\Omega} \mathbf{B}^T \mathbf{D} \epsilon^p(t - \Delta t) d\Omega$ are known.
2. Prediction for SBI boundary traction, T^s , using $u(t - \Delta t)$.
3. Elastic predictor step, $F^p(t) = F^p(t - \Delta t)$.
4. Solve linear system of equations for $u(t)$ and $T^f(t)$:

$$\mathbf{K}u - F^p + \mathbf{L}_f^T T^f + \mathbf{L}_s^T T^s = F$$

$$\mathbf{L}_f u = \mathbf{L}_d d$$

5. Corrector for SBI boundary traction using $\frac{1}{2}[u(t) + u(t - \Delta t)]$.
6. Plastic corrector: using radial return algorithm, compute $\epsilon^p(t)$ and $F^p(t)$.
7. Repeat steps 4 – 6 until error, $\frac{\|u^{n+1}(t) - u^n(t)\|}{\|u^{n+1}(t)\|} < tolerance$
8. Compute slip rate, V , using T^f from: $T^f + T_o^f = \sigma_e f(V, \theta) + \frac{\mu V}{2c_s}$
9. Estimate time increment based on slip rate and characteristic slip distance, $\Delta t = \min [C \frac{L}{V}]$ (Lapusta et al., 2000)
10. Update slip and state variable for next time step:

$$d(t + \Delta t) = d(t) + V(t)\Delta t$$

$$\dot{\theta}(t) = 1 - V(t) \theta(t)/L$$

$$\theta(t + \Delta t) = \theta(t) + \dot{\theta}(t)\Delta t$$

A fully dynamics solver with coupling of finite element and spectral boundary integral scheme is outlined in our previous studies (Mia et al., 2022; Abdelmeguid & Elbanna, 2022a, 2022b).

Table S1. List of parameters used in the simulations.

Parameter	Symbol	Values
Effective normal stress on fault	σ_n	50 MPa
Characteristic slip distance	L	500×10^{-6} m
Plate rate	V_p	10^{-9} m/s
Reference Slip rate	V_0	10^{-6} m/s
Initial slip rate	V_{init}	10^{-9} m/s
Reference friction coefficient	f_0	0.6
Shear wave speed	c_s	3464 m/s
Shear modulus	μ	32.038 GPa
Yield strength	σ_y	Variable
Nucleation length	L_{nuc}	100 m
Process zone size	R	21.36 m
Mesh size	dx and dy	0.5 m

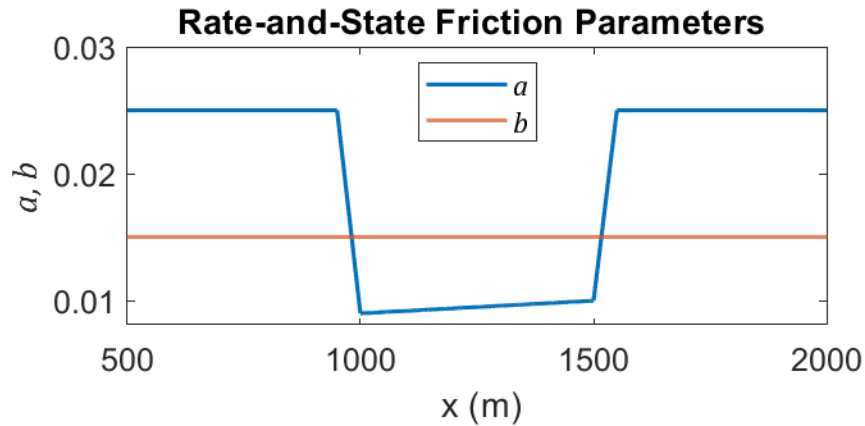
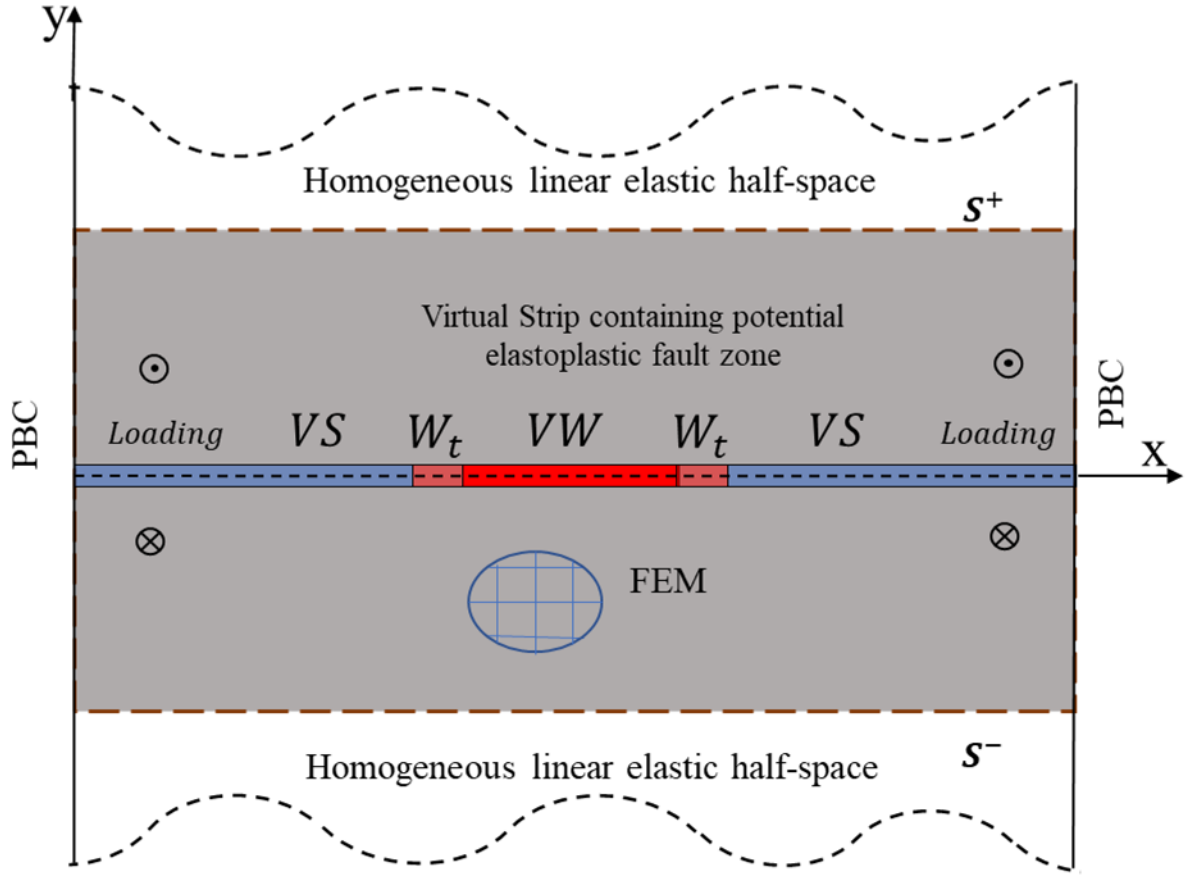


Figure S2. Model geometry and hybrid scheme set-up (Mia et al., 2019). 2D anti-plane rate-and-state fault contains seismogenic velocity weakening (VW) patch and creeping velocity strengthening (VS) patch with a transition region (W_t). Tectonic plate loading is applied through out of plane constant slip rate, $V_p = 10^{-9}$ m/s. Narrow virtual strip containing fault and potential elastoplastic bulk is discretized with FEM. Spectral Boundary Integral (SBI) replaces homogeneous linear elastic half spaces at the virtual boundaries (S^+ and S^-). Periodic Boundary Conditions (PBC) are applied at the lateral boundaries. Bottom figure shows the distribution of rate-and-state frictional parameters. a and b are non-negative dimensionless rate-and-state frictional parameters related to direct effect and state evolution respectively. Velocity weakening (VW) patch is associated with $a < b$ and velocity strengthening (VS) refers to $a > b$.

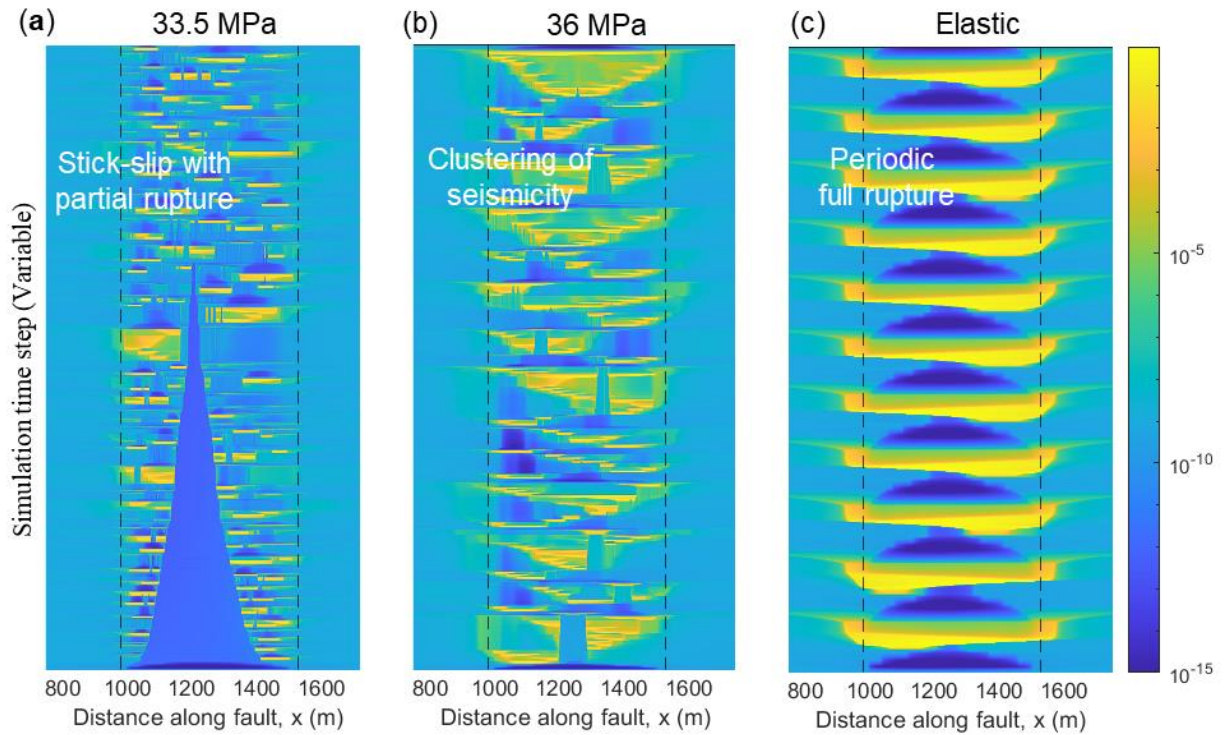


Figure S3. Results of fully dynamics simulation illustrating spatio-temporal evolution of slip rate. Patterns are qualitatively similar to the corresponding quasi-dynamics cases discussed in the main text. **(a)** Yield strength 33.5 MPa results in partial ruptures which successively unlock the central VW region and spread over the whole fault. **(b)** Relatively higher yield strength (36 MPa) shows clustering of seismicity. **(c)** Elastic case generates simple periodic fault spanning ruptures.

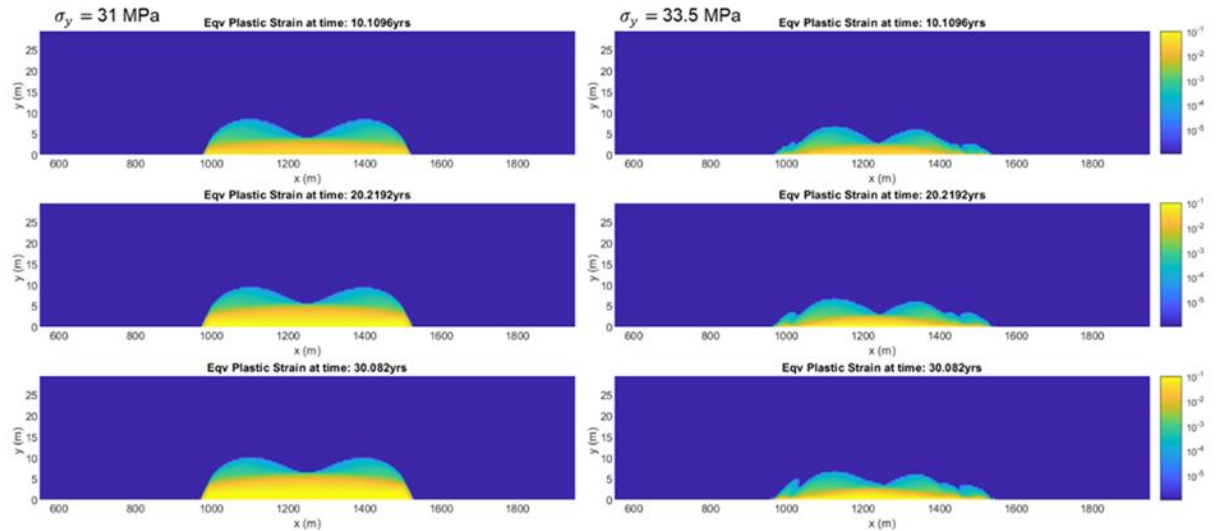


Figure S4. Equivalent plastic strain for yield strength 31 MPa and 33.5 MPa. Spatial extent of off-fault plasticity perpendicular to the fault plane is limited to narrow region close to the fault. Plasticity distribution is symmetric across the fault plane as the model is anti-plane with constant normal stress. Horizontally, plasticity spreads along the whole VW region of the fault.

References

- Aagaard, B. T., Knepley, M. G., & Williams, C. A. (2013). A domain decomposition approach to implementing fault slip in finite-element models of quasi-static and dynamic crustal deformation. *Journal of Geophysical Research: Solid Earth*, 118(6), 3059–3079. <https://doi.org/10.1002/jgrb.50217>
- Abdelmeguid, M., Ma, X., & Elbanna, A. (2019). A Novel Hybrid Finite Element-Spectral Boundary Integral Scheme for Modeling Earthquake Cycles: Application to Rate and State Faults With Low-Velocity Zones. *Journal of Geophysical Research: Solid Earth*, 124(12), 12854–12881. <https://doi.org/10.1029/2019JB018036>
- Abdelmeguid, M., & Elbanna, A. (2022a). Sequences of seismic and aseismic slip on bimaterial faults show dominant rupture asymmetry and potential for elevated seismic hazard. *Earth and Planetary Science Letters*, 593. <https://doi.org/10.1016/j.epsl.2022.117648>
- Abdelmeguid, M., & Elbanna, A. (2022b). Modeling Sequences of Earthquakes and Aseismic Slip (SEAS) in Elasto-Plastic Fault Zones With a Hybrid Finite Element Spectral Boundary Integral Scheme. *Journal of Geophysical Research: Solid Earth*, 127(12). <https://doi.org/10.1029/2022JB024548>
- Ben-Zion, Y., & Rice, J. R. (1997). Dynamic simulations of slip on a smooth fault in an elastic solid. *Journal of Geophysical Research: Solid Earth*, 102(B8), 17771-17784.
- Breitenfeld, M. S., & Geubelle, P. H. (1998). Numerical analysis of dynamic debonding under 2D in-plane and 3D loading. *International Journal of Fracture*, 93(1), 13-38.
- Dieterich, J. H. (1978). Time-dependent friction and the mechanics of stick-slip. *Pure and Applied Geophysics PAGEOPH*, 116(4-5), 790-806.
- Dieterich, J. H. (1979). Modeling of rock friction: 1. Experimental results and constitutive equations. *Journal of Geophysical Research: Solid Earth*, 84(B5), 2161-2168.
- Geubelle, P. H., & Breitenfeld, M. S. (1997). Numerical analysis of dynamic debonding under anti-plane shear loading. *International Journal of Fracture*, 85(3), 265-282.
- Geubelle, P. H., & Rice, J. R. (1995). A spectral method for three-dimensional elastodynamic fracture problems. *Journal of the Mechanics and Physics of Solids*, 43(11), 1791-1824.
- Lapusta, N., Rice, J. R., Ben-Zion, Y., & Zheng, G. (2000). Elastodynamic analysis for slow tectonic loading with spontaneous rupture episodes on faults with rate-and state-dependent friction. *Journal of Geophysical Research: Solid Earth*, 105(B10), 23765-23789.
- Mia, M. S., Abdelmeguid, M., & Elbanna, A. E. (2022). Spatio-temporal clustering of seismicity enabled by off-fault plasticity. *Geophysical Research Letters*, 49, e2021GL097601. <https://doi.org/10.1029/2021GL097601>
- Ranjith, K., & Rice, J. R. (1999). Stability of quasi-static slip in a single degree of freedom elastic system with rate and state dependent friction. *Journal of the Mechanics and Physics of Solids*, 47(6), 1207-1218.
- Rice, J. R. (1993). Spatio-temporal complexity of slip on a fault. *Journal of Geophysical Research: Solid Earth*, 98(B6), 9885-9907.

- Ampuero, J. P., & Rubin, A. M. (2008). Earthquake nucleation on rate and state faults - Aging and slip laws. *Journal of Geophysical Research: Solid Earth*, 113(1). <https://doi.org/10.1029/2007JB005082>
- Ruina, A. (1983). Slip instability and state variable friction laws. *Journal of Geophysical Research: Solid Earth*, 88(B12), 10359-10370.
- Simo, J. C., & Hughes, T. J. (2006). *Computational inelasticity* (Vol. 7). Springer Science & Business Media.